A memory-enhanced p-y model for piles in sand accounting for cyclic ratcheting and gapping effects

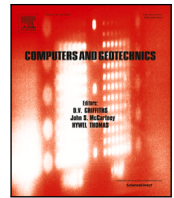Kementzetzidis, Evangelos; Pisano, Federico; Metrikine, Andrei V.

Important note
To cite this publication, please use the final published version (if applicable).
Please check the document version above.

Research paper

A memory-enhanced p-y model for piles in sand accounting for cyclic ratcheting and gapping effects

Evangelos Kementzetzidis, Federico Pisanò *, Andrei V. Metrikine

Faculty of Civil Engineering and Geosciences, Delft University of Technology, Stevinweg 1, Delft, 2628 CN, The Netherlands

ARTICLE INFO

ABSTRACT

The analysis of cyclically loaded piles is acquiring ever greater relevance in the field of geotechnical engineering, most recently in relation to the design of offshore monopiles. In this area, predicting the gradual accumulation of pile deflection under prolonged cycling is key to performing relevant serviceability assessments, for which simplified pile–soil interaction models that can be calibrated against common geotechnical data are strongly needed. This study proposes a new cyclic $p-y$ model for piles in sand that takes a step further towards meeting the mentioned requirements. The model is formulated in the framework of memory-enhanced bounding surface plasticity, and extends to cyclic loading conditions the previous monotonic, CPT-based $p-y$ formulation by Suryasentana and Lehane (2016); additionally, detailed modelling of pile–soil gapping is introduced to cope with the presence of unsaturated sand layers or, more generally, of cohesive soil behaviour. After detailed description of all model capabilities, field data from an onshore cyclic pile loading test are simulated using the proposed $p-y$ model, with the most relevant parameters calibrated against available CPT data. Satisfactory agreement is shown between experimental and numerical results, which supports the practical applicability of the model and the need for further studies on a fully CPT-based calibration.

1. Introduction

The use of piled foundations in civil engineering has evolved substantially over the past decades, with a number of new applications and design challenges driven by offshore energy developments (Kaynia, 2021). The viability of any piled foundation concept is closely related to the soundness and accuracy of the adopted analysis methods, especially for what concerns the interaction with the surrounding soil. For piles subjected to lateral loading, pile–soil interaction is most commonly analysed by resorting to the well-known $p-y$ method. The popularity of such approach is motivated by its simplicity and computational efficiency, in that it reduces the analysis of a 3D interaction problem to the study of a 1D foundation beam in the presence of distributed soil reactions (Winkler, 1867). In the $p-y$ framework, such soil reactions emerge from the constitutive behaviour of deformable soil spring elements, which yields a relationship between the lateral soil reaction (p) and corresponding pile deflection (y) at a given location (fully local approach). $p-y$ modelling approaches have significantly evolved in time with regard to mathematical formulation and calibration procedures, so as to accommodate a variety of geotechnical, geometrical, and loading conditions (API (American Petroleum Institute), 2011; DNV, 2014; Suryasentana and Lehane, 2016; Byrne et al., 2019).

The development of soil reaction models for cyclic loading conditions has been often associated with seismic design matters — see, e.g., the work of Boulanger et al. (1999), Brandenberg et al. (2013) and Choi et al. (2015) for piles in sandy soil. More recently, modern offshore wind developments have motivated new threads of soil–foundation interaction research, with focus on the impact of cyclic loading effects on the serviceability of offshore wind turbine foundations. A notable example is represented by the case of monopile foundations, which must be designed to avoid undesired resonance under environmental and mechanical loads (Kementzetzidis et al., 2018, 2019), as well as prevent the accumulation of excessive lateral tilt during their whole operational life (Arany et al., 2017). The prediction of such tilt requires thorough understanding of the role played by soil's ratcheting behaviour, especially when the pile at hand is subjected to asymmetric loading cycles (Niemunis et al., 2005; Cuéllar et al., 2009; Pisanò, 2019). In this respect, numerous experimental studies have been conducted in recent years — both in the laboratory (LeBlanc et al., 2010; Klinkvort et al., 2010; Klinkvort, 2012; Rudolph et al., 2014; Abadie, 2015; Zhu et al., 2016; Albiker et al., 2017; Wang et al., 2018; Frick and Achmus, 2019; Truong et al., 2019; Richards, 2019; Richards et al., 2021) and in the field (Li et al., 2015; Byrne et al., 2020a,b; Kementzetzidis et al., 2022). The data from such studies have provided essential input to the

---

* Corresponding author.
  E-mail address: f.pisano@tudelft.nl (F. Pisanò).

improvement of cyclic modelling procedures, ranging from advanced 3D analyses (Achmus et al., 2009; Jostad et al., 2014; Kementzetzidis et al., 2021; Staubach and Wichtmann, 2020; Liu et al., 2021) to, more recently, 1D $p - y$ approaches (Beuckelaers et al., 2020; Pisanò et al., 2022). However, there is still a substantial demand for enhanced cyclic $p - y$ models, since the majority of the existing cyclic formulations are typically unable to reproduce soil ratcheting effects and, therefore, the cyclic accumulation of pile deflection. This is the case, for example, of well-known $p - y$ formulations for monotonic loading (Matlock, 1970; DNV, 2014; Suryasentana and Lehane, 2016; Byrne et al., 2019), even when their cyclic versions are obtained based on the well-known Masing rules (Pyke, 1979); on the other hand, existing $p - y$ models for seismic applications (Boulanger et al., 1998; Choi et al., 2015) will often tend to over-predict the accumulated displacement when used to tackle cyclic loading conditions that are commonly experienced by offshore (mono)piles.

The practical use of $p - y$ models is intimately related to the possibility of calibrating relevant parameters against simple, readily available geotechnical data — such as those from standard laboratory and/or in-situ tests. In this regard, the $p - y$ models for piles in sand associated with, e.g., the API industry guidelines (API (American Petroleum Institute), 2011) and the PISA design method (Burd et al., 2020), require as an input, respectively, the friction angle (ϕ) and the initial relative density (D_r) of the sand. Since such properties are typically inferred from in-situ CPT results, an intermediate step is necessary to translate the measured resistance to cone penetration (q_c) into ϕ or D_r values — which adds a further layer of uncertainty to the overall calibration procedure. An interesting alternative is offered by so-called CPT-based $p - y$ methods, where model parameters are directly correlated to the q_c values measured in-situ (Novello, 1999; Dyson and Randolph, 2001; Suryasentana and Lehane, 2014b; Li et al., 2014). Particularly worth mentioning is the work of Suryasentana and Lehane (2014b, 2016), who proposed a CPT-based monotonic $p - y$ method that is applicable to piles of different cross-section shape and aspect ratio in (in)homogeneous sand profiles.

In the presence of cohesive soil behaviour, it is relevant to capture the occurrence and influence of pile–soil separation (also termed 'gapping'). Gapping entails the formation of a self-standing vertical soil surface as the pile is loaded away from a previous configuration with full pile–soil contact (Matlock et al., 1978; Suzuki and Nakai, 1985; Boulanger et al., 1999; Kementzetzidis et al., 2022). A number of gapping $p - y$ models are already available in the literature (Nogami et al., 1992; Boulanger et al., 1998, 1999; Gerolymos and Gazetas, 2005a,b; Hededal et al., 2010; Brandenberg et al., 2013), mostly in relation to seismic loading and clayey soil conditions. In the case of sandy soils, modelling pile–soil gapping may be relevant to simulating the effects of natural cementation and/or unsaturated conditions — in fact, most field testing campaigns about offshore monopiles have been recently carried out at onshore sites, and have returned measured pile responses that exhibit gapping effects (Li et al., 2015; Byrne et al., 2020a,b; Kementzetzidis et al., 2022).

Based on the above premises, this work aims to incorporate the following features into a new $p - y$ model for piles subjected to lateral cyclic loading in sand:

– hysteretic soil reaction behaviour, with controlled accumulation of lateral deflection under prolonged cyclic loading;
– modelling of pile–soil gapping effects under cyclic loading conditions;
– direct calibration of key $p - y$ model parameters against in-situ CPT data.

The proposed cyclic $p - y$ model is formulated in the framework of bounding surface plasticity (Dafalias, 1986), with the inclusion of an additional memory locus for the accurate modelling of lateral deflection accumulation under prolonged cycling (Corti et al., 2016; Liu et al.,

2019) – cyclic ratcheting soil behaviour. Further, the modelling of pile–soil gapping is inspired by the approach of Boulanger et al. (1998), who introduced a set of parallel springs to represent the physical mechanisms of 'frictional drag' and 'gap closure'. The model builds directly on the work of Suryasentana and Lehane (2016), in that their original CPT-based philosophy is extended to tackle cyclic loading conditions and pile–soil gapping effects.

After a detailed description of the mathematical formulation and its modelling implications, the suitability of the new $p - y$ model is finally assessed against original field data from recent medium-scale pile loading tests. In particular, the reference data describe the cyclic response of an instrumented tubular pile that was hammered into an inhomogeneous sand deposit including a shallow unsaturated layer (Tsetas et al., 2022; Kementzetzidis et al., 2022). While more data and further research will be necessary to further develop/validate the proposed CPT-based parameter calibration procedure, this paper demonstrates the remarkable capabilities and flexibility of the proposed $p - y$ model.

2. Bounding surface $p - y$ modelling with ratcheting control

This section describes the reformulation of the monotonic $p - y$ relationship by Suryasentana and Lehane (2016) as a bounding surface model with kinematic hardening. An additional ratcheting control mechanism is then introduced for more realistic simulation of pile deflection accumulation under prolonged cycling. The proposed model is applicable to one-directional cyclic loading scenarios with no substantial hydro-mechanical effects in the soil (i.e., drained conditions). Its implications are discussed in what follows both at the level of a single interaction element ($p-y$ spring) and global pile–soil interaction.

2.1. Reformulation of Suryasentana and Lehane's $p - y$ model

Suryasentana and Lehane proposed a monotonic $p - y$ relationship for piles in sand (henceforth referred to as *SL* model) along with a CPT-based parameter calibration procedure (Suryasentana and Lehane, 2014b, 2016). The *SL* model was developed after performing FE simulations of spherical cavity expansion and lateral pile loading, in order to establish quantitative relationships between simulated q_c values and lateral soil reactions for piles of different cross-section shape and aspect ratio — both in dry and water-saturated sand. The main outcome of Suryasentana and Lehane's work was a $p-y$ relationship between lateral soil reaction (p) and pile displacement (y), which (i) can be completely calibrated against in-situ q_c profiles, and (ii) has been successfully tested against the field data provided by Li et al. (2015), Suryasentana and Lehane (2014a, 2016), Anusic et al. (2019) and Wang et al. (2022). In particular, the *SL* $p - y$ relationship reads as follows:

$$p = p_u \left[1 - e^{-\alpha(y/D)^m} \right] \Rightarrow y = D \left[-\frac{1}{\alpha} \ln \left(\frac{p_u - p}{p_u} \right) \right]^{1/m} \quad (1)$$

In Eq. (1), p_u represents the ultimate soil reaction force per unit length, D is the pile diameter, while α (> 0) and m (> 0) are dimensionless parameters that can be calibrated using the following CPT-based relationships (Suryasentana and Lehane, 2016):

$$\begin{cases} p_u &= 2.4\sigma'_{v0} D \left(\dfrac{q_c}{\sigma'_{v0}} \right)^{0.67} \left(\dfrac{z}{D} \right)^{0.75} \leq q_c D \\ \alpha &= 8.9 \left(\dfrac{z}{D} \right)^{-1.25} \left(\dfrac{\sigma_{v0} - u_g}{\sigma'_{v0}} \right)^{0.5} \\ m &= 1 \end{cases} \quad (2)$$

where σ_{v0} and σ'_{v0} represent the in-situ total and effective vertical stresses at a depth z below the ground surface, while u_g is the hydrostatic pore water pressure at $z = 0$.

In what follows, the *SL* model is reformulated as a bounding surface plasticity model with kinematic hardening, which is suitable to tackle

cyclic loading conditions (Dafalias, 1986) – see also Choi et al. (2015). In the context of one-dimensional $p - y$ kinematic hardening plasticity, the following modelling ingredients are necessary to describe an incremental elasto-plastic response — for brevity, the terms 'stress' and 'strain' are used in lieu of 'soil reaction' (p, per unit length) and 'lateral displacement' (y):

(i) Elastic + plastic splitting of the strain increment

$$\mathrm{d}y = \mathrm{d}y_e + \mathrm{d}y_p \tag{3}$$

where the subscripts e and p denote the elastic and plastic components of the total strain increment, respectively.

(ii) Elastic law

$$\mathrm{d}y_e = \frac{\mathrm{d}p}{K} \tag{4}$$

where the stiffness K relates the corresponding increments of stress and elastic strain.

(iii) Translating yield locus (kinematic hardening)

$$f = |p - p_\alpha| - p_y = 0 \tag{5}$$

Eq. (5) defines a translating locus in the 1D stress space, always centred around the (evolving) back-stress p_α with a total size equal to $2 \cdot p_y$. Under a given loading history, the back-stress is assumed to evolve with the plastic strain increment according to the following

(iv) Back-stress translation rule

$$\mathrm{d}p_\alpha = H \cdot \mathrm{d}y_p \tag{6}$$

where H is the so-called plastic modulus. In the spirit of bounding surface plasticity, H is set to depend on the distance between the current stress p and its projection (along the loading direction) onto the following

(v) Bounding locus

$$F = |p| - p_u = 0 \tag{7}$$

which identifies the range of admissible stresses, i.e., $-p_u \leq p \leq p_u$.

(vi) Flow rule

$$\mathrm{d}y_p = \mathrm{d}\lambda \cdot \mathrm{sgn}\left(p - p_\alpha\right) \tag{8}$$

where sgn denotes the signum function and the plastic multiplier $\mathrm{d}\lambda$ is obtained through the 'consistency condition' ($\mathrm{d}f = 0$) whenever the yield condition $f = 0$ is satisfied.

To enable perfect adherence to the original *SL* relationship, two further assumptions are embedded into the model formulation:

1. negligible elastic strains ($\mathrm{d}y_e = 0$), i.e., $K \to \infty$ and $\mathrm{d}y_p = \mathrm{d}y$;
2. plastic straining occurring from the very onset of loading, which coincides with the assumption of 'zero elastic range', i.e., $p_y \to 0$ (Dafalias and Popov, 1977; Borja and Amies, 1994; Pisanò and Jeremić, 2014).

Introducing the assumption 2 into Eq. (5) implies that

$$p = p_\alpha \Rightarrow \mathrm{d}p = \mathrm{d}p_\alpha \tag{9}$$

which, in combination with the translation rule (6), leads to the following 'hypoplastic' redefinition of the flow rule (8):

$$\mathrm{d}y_p = \frac{\mathrm{d}p}{H} \tag{10}$$

and, in light of assumption 1, to the final relationship between strain and stress increments below:

$$\mathrm{d}y = \frac{\mathrm{d}p}{H} \Rightarrow y = \int \frac{1}{H} \mathrm{d}p \tag{11}$$

In conclusion, the performance (and accuracy) of the resulting model depends entirely on the choice of the hardening modulus H. In order to reproduce within the reference plasticity framework the monotonic $p - y$ relationship (1), the following expression of H is derived using Eq. (11):

$$H = \frac{\alpha \cdot m}{D} \cdot |\bar{p}_u - p| \cdot \left| \frac{1}{\alpha} \ln \left(\frac{\bar{p}_u - p}{\bar{p}_u - p_0} \right) \right|^{\frac{m-1}{m}} \tag{12}$$

which underlies a $p - y$ model suitable for the step-by-step analysis of cyclic pile–soil interaction problems in the time domain. In Eq. (12), $\bar{p}_u = p_u \cdot \mathrm{sgn}(\mathrm{d}p)$ with $\mathrm{d}p$ denoting the stress increment within the current calculation step; p_0 represents a stress projection centre that takes the current p value whenever a stress reversal occurs (i.e., whenever $\mathrm{sgn}(\mathrm{d}p)$ changes[1]). For $0 < m < 1$, Eq. (12) complies with well-established bounding surface plasticity principles, in that $H \to 0$ when $p \to \bar{p}_u$ (nil plastic stiffness as the bounding locus is approached) and $H \to \infty$ when $p \to p_0$. The limit setting $m = 1$ suggested by Suryasentana and Lehane (2016) (Eq. (2)) can be approximated as closely as desired by choosing values slightly lower than 1 (e.g., $m = 0.9999$), so as to preserve the aforementioned limiting properties of the plastic modulus — which would no longer hold for m strictly equal to 1. Importantly, the bounding surface model resulting from Eq. (12) (with p_0 initialised to 0) can easily be proven to match the *SL* relationship for monotonic loading conditions — see Fig. 2.

2.2. Memory-enhancement for ratcheting control

As noted in the introduction, the study of soil–structure interaction in the presence of ratcheting soil behaviour is key to analysing the serviceability of offshore monopiles (Wichtmann et al., 2010; Cuéllar et al., 2012; Liu et al., 2021), and is at the heart of the experimental studies cited above. The same subject has also been attracting the interest of numerical modellers, who have recently begun to propose $p - y$ approaches accounting for cyclic ratcheting effects — see, e.g., the work of Beuckelaers et al. (2020) in the framework of hyperplasticity.

Bounding surface models of the kind described in Section 2.1 are known to be quantitatively inaccurate with regard to the simulation of cyclic ratcheting — particularly, they tend to overpredict the accumulation of ratcheting deformations under (asymmetric) cyclic loading. In order to overcome this drawback, the above bounding surface $p - y$ formulation is enriched with an additional 'memory locus', which can be exploited to keep track of the cyclic stress history and make the stiffness of the system evolve in agreement with relevant experimental evidence. The same approach has been recently developed for the constitutive modelling of (multiaxial) cyclic sand behaviour (Corti et al., 2016; Liu et al., 2019, 2020), and is here applied for the first time to 1D $p - y$ modelling. The use of a memory locus (Eq. (13)) that keeps track of the previous loading history allows higher versatility than casting fabric change effects directly into the evolution of the bounding domain (Eq. (7)), particularly with regard to complex cyclic loading histories (Liu et al., 2022).

The memory-enhancement of the above bounding surface $p - y$ model requires the introduction of the following memory locus:

$$F_M = |p - p_{\alpha,M}| - p_M = 0 \tag{13}$$

which can translate and change in size in the stress space through the evolution of the associated memory back-stress ($p_{\alpha,M}$) and domain size (p_M), respectively. The memory locus is used to introduce an additional metrics into the model, namely the distance b_M between the current stress p and its projection onto the memory locus ($\bar{p}_M$) along the loading direction ($\bar{p}_M = p_{\alpha,M} + \bar{p}_M$, with $\bar{p}_M = p_M \cdot \mathrm{sgn}(\mathrm{d}p)$):

$$b_M = |p - \bar{p}_M| \tag{14}$$

---

[1] The value of p_0 for each $p - y$ spring is usually initialised to 0, and then varies during the analysis as many times as the number of stress reversals.
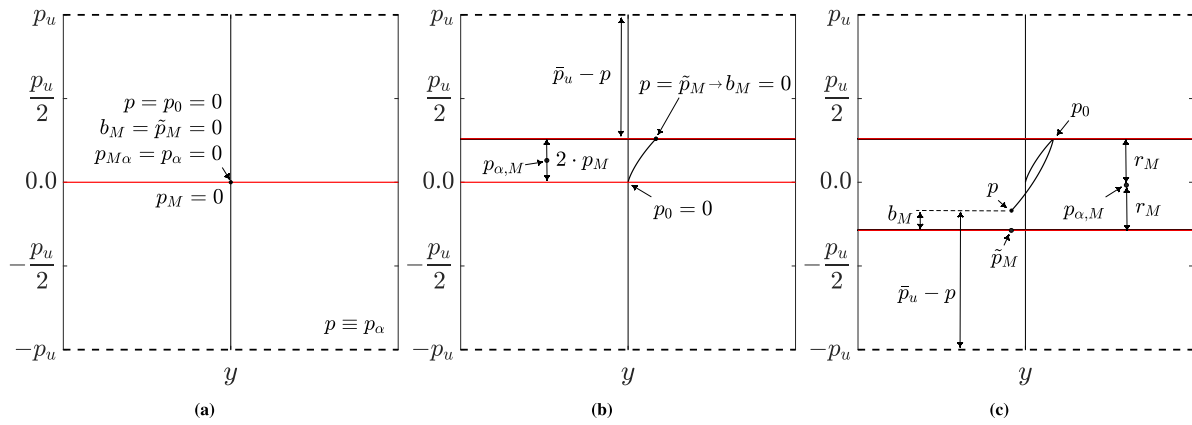
Fig. 1. Location and evolution of the model loci in the proposed memory-enhanced bounding surface $p - y$ formulation.

The distance b_M is then exploited to upgrade the definition of the plastic modulus H in Eq. (12) as follows:

$$H_M = H \cdot \exp\left\{\mu_0\left(\frac{b_M}{b_{ref}}\right)^2\right\} \qquad (15)$$

where μ_0 is a scalar ratcheting-control parameter, and $b_{ref} = 2p_u$ is introduced for normalisation purposes.

The role of the memory locus can be grasped through Eq. (15): when the current stress point satisfies $F_M = 0$, i.e., $b_M = 0$, then $H_M = H$ and the response is not affected by the memory mechanism — this situation is referred to as 'virgin loading conditions'; in contrast, $H_M > H$ whenever p lies inside the memory locus, which implies a stiffer response depending on the current value of b_M and the selected parameter μ_0. As is shown in the following, the addition of the memory locus can improve the modelling of cyclic ratcheting, after introducing suitable evolution laws for the memory internal variables $p_{\alpha,M}$ and p_M (mixed isotropic–kinematic hardening). Herein, the same approach described by Liu et al. (2019) is adapted to 1D $p - y$ modelling, which is summarised by the following two assumptions:

1. starting from an initial situation of virgin loading (i.e., $p = \tilde{p}_M$) with $p_M = 0$, the evolution of p under first loading (and under any following virgin loading event) produces an expansion of the memory locus ($dp_M > 0$) along dp, pivoting around the opposite boundary point of the locus itself;
2. the mathematical relationships derived based on the above assumption are held valid for any loading conditions (i.e., also for $p \neq \tilde{p}_M$).

These assumptions underlie the simple derivations reported in Appendix A, which lead to the following evolution laws for $p_{\alpha,M}$ and p_M:

$$dp_{\alpha,M} = \tilde{H}_M \cdot dy_p \qquad (16)$$

$$dp_M = |dp_{\alpha,M}| \qquad (17)$$

where $\tilde{H}_M$ is a 'memory' hardening modulus related to a fictitious deformation mechanism built on the evolving memory locus (Corti et al., 2016; Liu et al., 2019) – cf. to Eq. (6).

Fig. 1 illustrates the location and evolution of the different model loci during an arbitrary loading–unloading one-directional $p-y$ process, which determines the update of the projection centre p_0 upon load reversal (Eq. (12)) – also note that, due to the vanishing yield locus, $p \equiv p_\alpha$ (Eq. (9)). Given the phenomenological nature of the memory locus, its initialisation at the beginning of a $p - y$ analysis is usually such that $p_{\alpha,M} = p_\alpha \equiv p(= 0)$ and $p_M = 0$. The assumption of 'initially virgin loading' may be relaxed by setting $p_M > 0$ at the onset of lateral loading, for instance to simulate the influence of pile installation effects

on the lateral stiffness. Although appealing, this possibility will require further studies on how to convert pile driving effects into a suitable initialisation of the memory locus for simplified $p - y$ analyses.

2.3. From memory-enhanced $p - y$ modelling to cyclic pile response

The memory-enhanced $p-y$ model – as well as its gapping extension (see Section 3) – was implemented as a material model for *ZeroLength* elements into the OpenSees Finite Element (FE) platform (McKenna, 2011). In all pile–soil interaction analyses presented herein, the step-by-step integration of the above $p - y$ equations was performed using a fifth-order Runge–Kutta integration scheme with adaptive time step and automatic error control — in which the local truncation error is estimated as the difference between sixth- and fifth-order solution estimates, as detailed by Sloan et al. (2001).

It is worth recalling that the memory-enhanced $p - y$ model features at the same time (i) a zero yield locus and (ii) infinite elastic stiffness. Although perfectly admissible from a theoretical standpoint, such features require special care with regard to numerical integration. In particular, a practical 'cut-off' (upper bound) was introduced on the theoretically infinite value of the unloading/reloading stiffness, which was found to negligibly impact the intended *SL* monotonic backbone curve. Moreover, given the adopted bounding surface plasticity framework, the $p - y$ model suffers from the well-known 'overshooting' phenomenon, which can produce unrealistically large stiffness values upon unloading/reloading cycles of small amplitude — such occurrence was originally recognised by Dafalias (1986) as an inherent shortcoming of the bounding surface plasticity theory. Herein, overshooting effects have been remedied following the methodology proposed by Dafalias and Taiebat (2016).

Fig. 2 illustrates the role of the memory mechanism in the response of a single $p - y$ spring in terms of normalised stress–strain variables (i.e., p/p_u vs y/y_{ref}, where y_{ref} denotes the spring deformation associated with the maximum p/p_u value attained monotonically for a given cyclic loading scenario — in Fig. 2 y_{ref} is associated with $p/p_u = 0.5$). In particular, the behaviour under asymmetric/one-way (Fig. 2(a)) and symmetric/two-way (Fig. 2(b)) loading is exemplified for $\mu_0 = 0$, 50, 500 – note that $\mu_0 = 0$ implies $H_M = H$ (Eq. (15)) and, therefore, no memory effects. As expected, an increase in μ_0 determines a lower cyclic accumulation of the spring strain under one-way loading, while a decrease in the net lateral deformation is observed under a symmetric excitation. The one-way behaviour in Fig. 2(a) appears to capture the gradual stiffening of the soil response under prolonged cyclic (in reality largely due to cyclic densification), which would not be possible to reproduce through traditional bounding surface modelling (Corti et al., 2016; Liu et al., 2019). It should be noted that, in the proposed formulation, the memory locus does not influence the ultimate resistance associated with the local soil reactions – i.e., p_u is not altered by cyclic
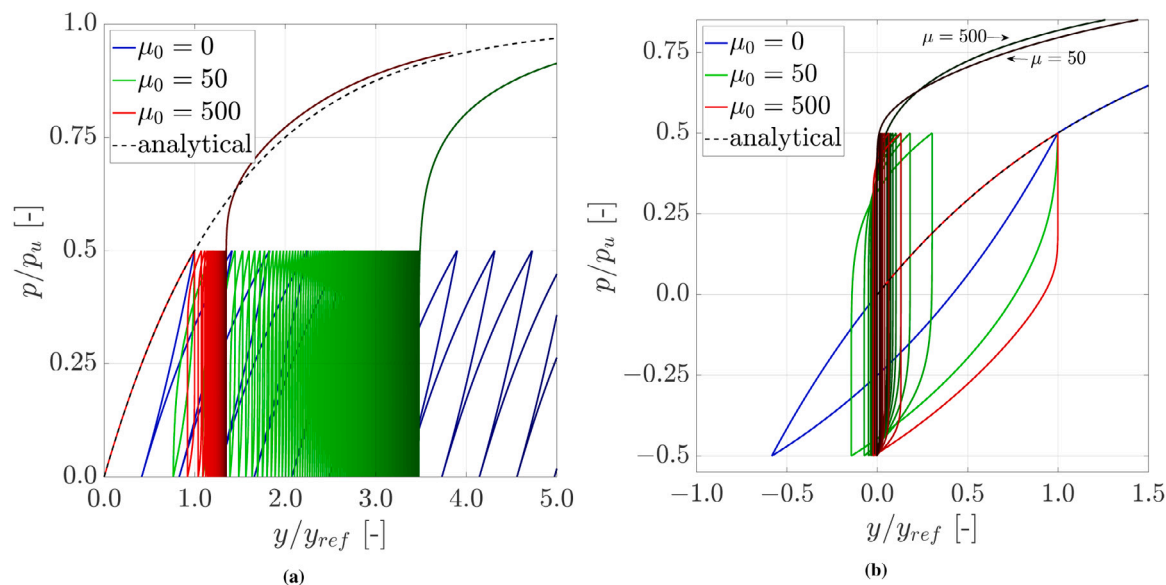
Fig. 2. Cyclic performance of the memory-enhanced bounding surface $p-y$ model under (a) asymmetric/one-way cyclic loading ($N = 100$ cycles), and (b) symmetric/two-way loading ($N = 10$ cycles) for $\mu_0 = 0, 50, 500$. The black dashed line represents the SL analytical relationship in Eq. (1); lines associated with $\mu_0 = 50, 500$ gradually darken as the number of loading cycles increases. All model parameters calibrated based on Eq. (2) for a circular pile (diameter: $D = 0.762$ m) and a soil location characterised by: $z = 4$ m (soil depth), cone resistance $q_c = 17$ MPa, dry unit weight $\gamma_{dry} = 16$ kN/m³).

loading. This modelling choice is consistent with experimental evidence from the literature (Abadie et al., 2019; Richards et al., 2021), showing that the monotonic capacity of a pile in sand is mostly unaffected by previous loading cycles of lower amplitude (and same direction). In Figs. 2(a), 2(b), the first loading branch obtained through numerical integration perfectly matches, as intended, the *SL* $p-y$ relationship (black dashed line in the figure) (Suryasentana and Lehane, 2016). Importantly, since inelastic deformations accumulate as part of a single plastic strain component (y_p), there is no need to calibrate different model parameters for either monotonic or cyclic loading histories — that is a typical shortcoming of modelling the cyclic accumulated strain as an additional component of inelastic deformation (Beuckelaers et al., 2020).

The implications of the proposed model in scaling up from a single $p-y$ element to the global pile–soil system are exemplified with respect to the laterally loaded tubular pile in Fig. 3(a), featuring total and embedded lengths equal to $L = 9$ m and $L_e = 8$ m, diameter $D = 0.762$ m, and wall thickness $h = 1.59$ cm — the lateral load is applied with an eccentricity $e = 1$ m with respect to the ground surface ($z = 0$). In the corresponding OpenSees simulations of the pile subjected to one-way and two-way cyclic loading, the pile was uniformly discretised using 90 *ElasticTimoshenkoBeam* elements with typical elastic ($E = 210$ GPa, $v = 0.3$) and cross-sectional properties (Timoshenko shear coefficient: $\kappa = 0.57$, from Hutchinson, 2001), while nodal soil reactions compliant with the memory-enhanced $p-y$ model were introduced along the embedded pile length with a spacing of $\Delta z = 0.08$ m. Since this work focuses on lateral $p-y$ reactions, additional reaction mechanisms that may become prominent for lower L/D ratios – e.g., distributed moment, base shear resistance and moment fixity (Davidson, 1982; Lam and Martin, 1986; Gerolymos and Gazetas, 2006; Byrne et al., 2019) – were deliberately neglected in this first demonstration of the model. A set of meaningful $p-y$ parameters was obtained for a fictitious cone resistance profile – namely q_c[MPa] $= 5 + 2z$, with z in metres – using the calibration procedure in Eq. (2) (with $m = 0.9999$ instead of $m = 1$), and setting $\mu_0 = 20$ for the ratcheting control mechanism.

Qualitatively, the resulting load–displacement response of the pile at the ground surface resembles in most respects the evidence emerging from the aforecited experimental studies on monopiles under lateral cyclic loading. For instance, in the case of one-way loading (Fig. 3(b)),

the typical gradual decrease in deflection accumulation rate is observed, along with an increase in the secant cyclic stiffness and a decrease in the cyclic loop area associated with subsequent response cycles (Abadie et al., 2019). Under symmetric/two-way loading (Fig. 3(c)), a net shift towards negative pile head deflection values is observed, which is consistent with recent observations from centrifuge experimental tests (Richards et al., 2021) and more advanced 3D FE simulations (Liu et al., 2021).

3. Modelling of cyclic pile–soil gapping

Most onshore sites feature a phreatic level that is located at a certain depth below the ground surface, which determines a water saturation degree lower than 1 in the shallowest soil layers. As is well-known, unsaturated soils exhibit features of cohesive behaviour due to (transient) hydraulic suction effects, even in geomaterials that would otherwise be cohesionless — such as sands (Fredlund, 2006). The pseudo-cohesion of unsaturated sand can (temporarily) enhance the stability of relatively steep slopes, or enable the formation of a shallow gap with the soil in laterally loaded piles. In the latter case, cyclic soil reaction curves ($p-y$) are expected to assume a sort of S-shape, similar to that previously described for cohesive clayey soils — see Fig. 4. Importantly, gapping effects under cyclic loading conditions are inherently displacement-dependent, as are the evolution of the gap depth and the alternation of 'contact'-'no-contact' stages between the pile and the soil. Pile–soil gapping mechanisms are more extensively described, e.g., by Matlock et al. (1978), Suzuki and Nakai (1985), Boulanger et al. (1999) and Kementzetzidis et al. (2022).

The memory-enhanced $p-y$ model described in the previous section is applicable to cyclically loaded piles in either dry or fully saturated sand. In order to reproduce gapping effects in unsaturated sand, an extension of the modelling framework is proposed hereafter. To this end, the overall soil reaction scheme (henceforth the gapping $p-y$ model) is extended as is shown in Fig. 5, based on the following general principles:

– under one-directional cyclic loading, soil reactions must be modelled separately on the two sides – say, left (L) and right (R) – of the pile, due to the asymmetric configuration and evolution of the gap (Heidari et al., 2014). This is at variance with usual $p-y$
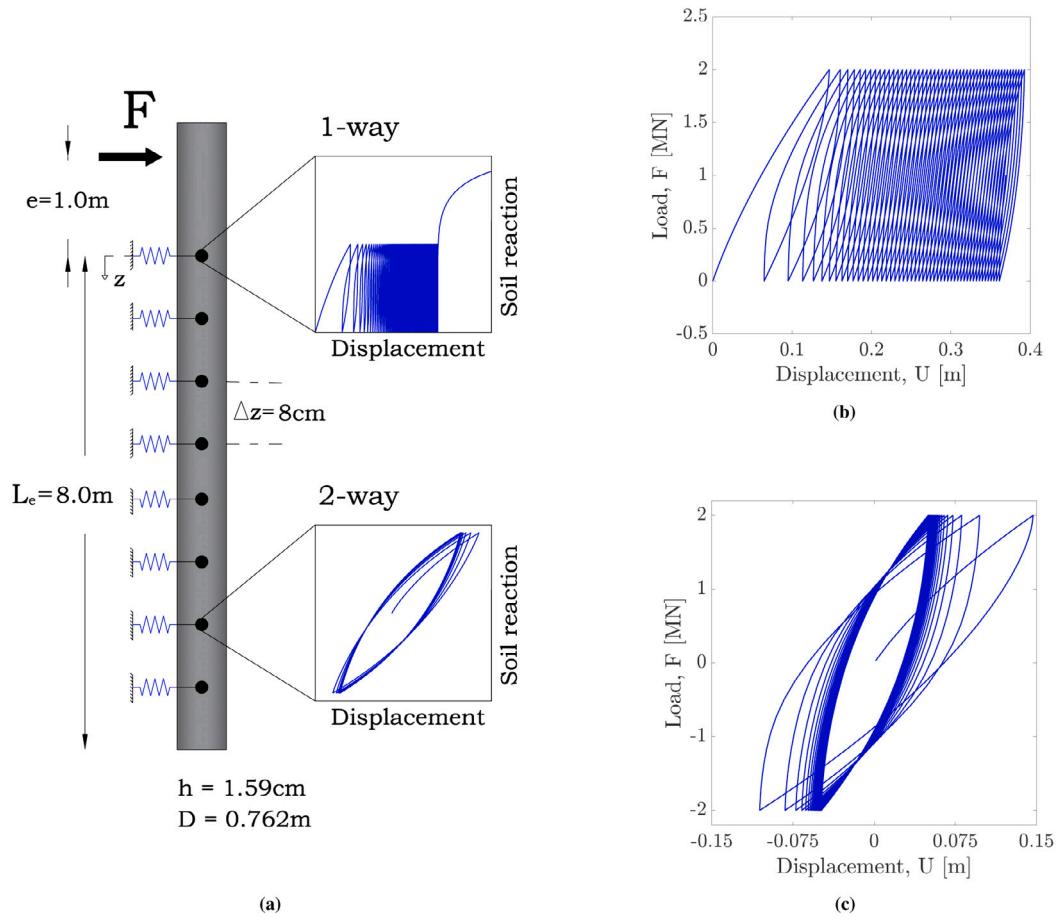
Fig. 3. (a) Reference pile subjected to lateral cyclic loading: typical one-way vs two-way responses of the soil reaction springs in agreement with the proposed memory-enhanced $p - y$ formulation; simulated load–displacement pile response at ground surface to (b) one-way and (c) two-way cyclic loading ($N = 50$ loading cycles) with regard to the reference pile in (a).
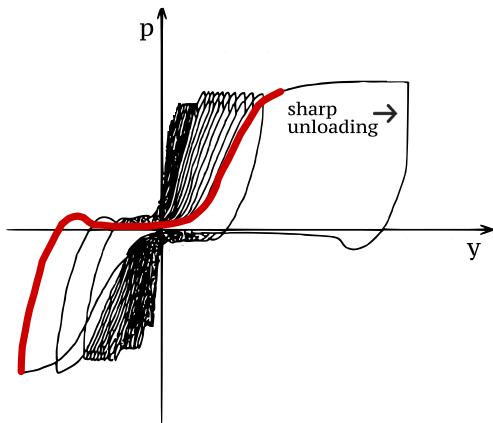

Fig. 4. Cyclic $p - y$ curves for cohesive soils. The red line highlights the mentioned S shape of the last $p - y$ response cycle.
Source: Modified after Randolph and Gourvenec (2011), originally from Bea et al. (1979).

formulations, where soil reactions at a given depth represent the total integral along the perimeter of the foundation;

– on each side of the pile, a multi-component soil reaction scheme is introduced (Fig. 5), including (i) the memory-enhanced $p - y$ mechanism described in Section 2 (henceforth the memory component) and three additional elements referred to as (ii) 'separation', (iii) 'closure', and (iv) 'drag' springs.

In particular, the memory component is connected in parallel to the separation spring to form a so-called 'soil element', which is in turn

Table 1
Static and kinematic relationships for the spring elements included in the gapping $p - y$ model (Fig. 5).

Spring	Reaction	Deflection
Soil	$p_m + p_{sp} = p_s$	$y_{sp} = y_m = y_s$
Gap	$p_d + p_c = p_g$	$y_d = y_c = y_g$
Left/right	$p_g = p_s = p_L \; \Vert \; p_R$	$y_g + y_s = y_R = y_L$
$p - y$	$p_L + p_R = p$	$y_R = y_L = y$

linked in series to a parallel combination of the closure and drag springs (altogether the 'gap' spring). The resulting $p - y$ scheme combines the soil and gap elements, both including two distinct sub-components. In what follows, the static and kinematic variables associated with each soil reaction component are denoted by specific subscripts (memory spring → m; separation spring → sp; soil spring → s; drag spring → d; closure spring → c; gap spring → g; left component → L; right component → R), while typical relationships for the springs connected either in series or in parallel are reported in Table 1. For the sake of clarity, the physical motivation and mathematical formulation of each model component are first individually described in the following sub-sections; then, the global performance of the model is discussed in detail, particularly with respect to the cyclic lateral response of a pile embedded in a combination of unsaturated and saturated sand layers.

3.1. Impact of gap modelling features on $p - y$ response

The model components displayed in Fig. 5 are hereafter described in light of the following remarks:
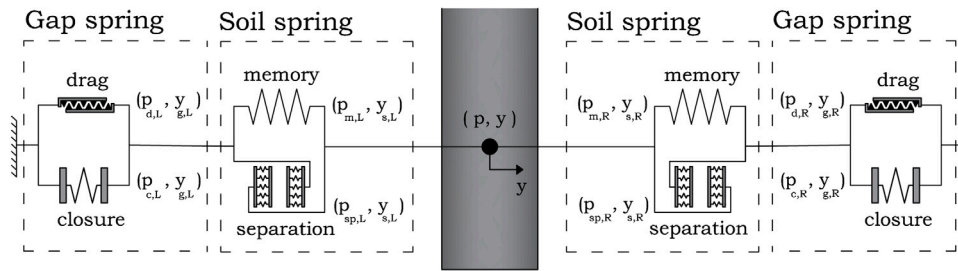
Fig. 5. Proposed $p - y$ scheme allowing for cyclic ratcheting control and pile–soil gapping.

– all relevant internal variables (such as the maximum displacement ever experienced at one location, y_{max}) are defined independently for each side of the pile, and denoted by above-mentioned subscripts L and R;

– at a given soil depth, the size of the gap opening is determined by the pile displacement history, and assumed to coincide with the interval $[y_{L,max}, y_{R,max}]$, which is updated every time either $y_{L,max}$ or $y_{R,max}$ varies;

– under general cyclic loading conditions, the gap spring is activated or deactivated depending on whether the pile and the soil are or are not in contact. On each side of the pile, pile–soil contact results in deactivation of the gapping spring, which is then re-activated when pile–soil separation occurs again (on the corresponding side).

Regarding the third item in the above list, the response of the gap spring is computed according to the following geometrical cases:

1. the pile and the soil are in contact on the right side (i.e., $y = y_{R,max}$ and the right gap spring is inactive), hence, upon rightward loading, the left side of the pile lies inside the gap while $y > y_{L,max}$;

2. the pile and the soil are in contact on the left side (i.e., $y = y_{L,max}$ and the left gap spring is inactive), hence, upon leftward loading, the right side of the pile lies inside the gap while $y < y_{R,max}$;

3. both sides of the pile are within the gap, i.e., $y_{L,max} < y < y_{R,max}$.

The interaction elements in Fig. 5 are hereafter individually described in the following order: (i) separation spring, (ii) closure spring, and (iii) combination of drag and memory springs. Note that, although presented last in what follows, the (novel) features of the memory element are identical to those of the memory-enhanced $p - y$ model described in Section 2 for piles in dry or saturated sand — with only some minor differences related to the adjusted limit resistance p_u ($p_{u,m}$ in the gapping $p-y$ model) in the presence of the additional drag spring. Using the model requires the calibration of the nine parameters listed in Table 2, which is further discussed in the following section.

3.1.1. Separation spring

Due to the occurrence of pile–soil separation during gapping, soil reaction curves for piles in unsaturated sand are known to exhibit certain unique features, such as a sharp unloading branch in force–displacement plane — precisely at the onset of the separation stage (Fig. 4). This kind of behaviour is enabled by the aforementioned pseudo-cohesion, which also tends to limit displacement relaxation in the associated soil reaction curve upon load reduction. Sharper unloading branches are reproduced by the gapping $p - y$ model for unsaturated conditions via a dedicated separation spring that is set in parallel with the memory element, and stiffens during unloading (i.e., when $|y|$ decreases with respect to $|y_{max}|$) to induce a globally stiffer unloading–reloading response. From a mathematical standpoint, the separation spring stiffness K_{sp} is expressed as follows — recall that

the separation and the memory elements share the same displacement y_s (Table 1) as parts of the combined 'soil spring':

$$K_{sp} = \begin{cases} 0 & y_s = y_{s,max} \\ M_{sp}\alpha_{sp}K_{50}\left[1 - \dfrac{1}{\beta_{sp}\left(\dfrac{y_{s,max}-y_s}{z}\right)^2 + 1}\right] & |y_s| < |y_{s,max}| \end{cases} \tag{18}$$

where z is the soil depth, K_{50} is the stiffness of the parallel memory spring at $p = 0.5p_{u,m}$, while α_{sp}, M_{sp}, and β_{sp} are scalar factors to be calibrated.

In summary, the separation spring has only two possible response modes: (i) it is inactive when $y_s = y_{s,max}$, i.e., when the pile and the soil are (or go back to be) in contact; (ii) it stiffens progressively for increasing $|y_s - y_{s,max}|$ values (pile–soil separation) up to the limiting value of $K_{sep} = M_{sp}\alpha_{sp}K_{50}$. M_{sp} is a stiffness multiplier factor always larger than 1, which aims to preserve the same relative contribution to the soil reaction of the separation and memory springs during the whole loading history — note that the memory spring will gradually stiffen under repeated loading cycles. To this end, M_{sp} is given a value that represents the status of the memory mechanism (e.g., the current size of the memory locus normalised by the memory spring capacity – i.e., $p_M^{cur}/p_{u,m}$) each time that the separation spring is activated, which happens upon the transition from $y_s = y_{s,max}$ to $|y_s| < |y_{s,max}|$.

In addition to stiffening the unloading–reloading response of the soil element, the stiffness of the separation spring also works to limit the reaction force of the memory element when $|y_s| < |y_{s,max}|$ – i.e., when a certain side of the pile is moving inside the gap. With such a reaction limitation it is effectively possible to inhibit the evolution of the internal variables $p_{\alpha,M}$ and p_M associated with the memory mechanism (see Eqs. (17)–(16)). This is in fact a desirable feature for this component of the soil reaction, since the soil fabric changes (e.g., densification) induced by cyclic loading – and phenomenologically described through the memory mechanism – are mostly driven by plastic straining, which evolves differently depending on whether the pile and the soil are or are not in contact.

The impact of the separation stiffness on the cyclic response of the soil element is illustrated in Fig. 6(a). The response of the soil spring for $\alpha_{sp} = 0$ is presented in blue, in which case the soil element reduces to the sole memory component; in contrast, the red curve represents the case of $\alpha_{sp} = 2$. Increasing values of α_{sp} lead to a stiffer soil spring response inside the gap, accompanied by a reduced contribution of the memory component (red dotted line versus blue solid line). Under repetitive cycling, and depending on the selected μ_0 value, the unloading stiffness of the soil spring will naturally increase in time – see Fig. 2 – up to reproducing the desired sharp unloading response that emerges from pile–soil gapping. In such cases, setting $\alpha_{sp} = 0$ may be assumed as an easier calibration option, considering though that memory effects will invariably develop regardless of pile–soil contact/separation.

Table 2

Gapping $p - y$ model parameters along with their suggested range (for preliminary calibration) and calibrated values for the field test results in Section [4] – the recommended values in the second column for p_u, α, and m are based on Suryasentana and Lehane ([2016]). $\bar{\sigma}_0'$ represents the in-situ mean effective stress, while $\bar{\sigma}_{ref} = 100$ kPa is a reference pressure. For case example in Section [4], identical memory spring parameters have been set both above (unsaturated soil) and below (saturated soil) the assumed water table depth.

	Recommended values/range	Case example in Section [4]	Units
CPT-based spring capacity			
p_u	$2.4\sigma_{v0}' D \left(\dfrac{q_c}{\sigma_{v0}'}\right)^{0.67} \left(\dfrac{z}{D}\right)^{0.75}$	$0.34\sigma_{v0}' D \left(\dfrac{q_c}{\sigma_{v0}'}\right)^{0.67} \left(\dfrac{z}{D}\right)^{0.75}$	[N/m]
Memory spring			
$p_{u,m}$	$(1 - C_d)p_u$		[N/m]
α	$8.9 \left(\dfrac{z}{D}\right)^{-1.26} \left(\dfrac{\sigma_{v0} - u_g}{\sigma_{v0}'}\right)^{0.5}$		[–]
m	$0.9999...99 \rightarrow 1.0$	0.5	[–]
μ_0	to be calibrated	$7.7 \times 10^4 \exp\left\{6\dfrac{\bar{\sigma}_0' - \bar{\sigma}_{ref}}{\bar{\sigma}_{ref}}\right\}$	[–]
Separation spring		(Deactivated)	
α_{sp}	$0 - 5$	0	[–]
β_{sp}	$> 10^6$	–	[–]
M_{sp}	$p_M^{cur}/p_{u,m}$	–	[–]
Drag spring		(Deactivated)	
C_d	$0–1$	0	[–]
$p_{u,d}$	$C_d p_u$	–	[N/m]
Closure spring			
m_c	0.6	0.5	[–]
α_c	20	$-ln(0.15)/(0.55)^{m_c}$	[–]

3.1.2. Closure spring

The inclusion of the so-called closure spring is needed to simulate the peculiar shape (resembling an inverted S) of the stress–strain response cycles in the presence of cohesive soil behaviour (Boulanger et al., 1999) – also shown in Fig. 4. To reproduce mathematically such a shape, the following function – similar to Eq. (1) – is adopted to relate, in finite terms, the reaction component in the closure spring (p_c) to the corresponding displacement (y_g, i.e., the overall gap spring displacement):

$$p_c = p_{c,max}\,\mathrm{e}^{-\alpha_c\left|\frac{y_g - y_{g,0}}{y_{max}}\right|^{m_c}} \qquad (19)$$

where m_c and α_c are dimensionless shape parameters, while $y_{g,0}$ assumes the current value of y_g every time the pile re-enters the gap from a new y_{max} ($y_g - y_{g,0} = 0$, when also $p_c = p_{c,max}$). On each side of the pile, y_g and p_c evolve independently, as implied by the sketch in Fig. 5. Independent on each side is also the update of the internal variables ($y_{L-R,max}$, $y_{g,L-R,0}$, $p_{c,L-R,max}$, which occurs as follows when a cross-section of the pile at a given depth re-enters the gap (upon unloading) after the attainment of a new maximum y value, y_{max}:

$$y_{g,R,0} = y_{g,R} \quad \| \quad y_{g,L,0} = y_{g,L} \qquad (a)$$

$$y_{R,max} = y \quad \| \quad y_{L,max} = y \qquad (b)$$

$$p_{c,R,max} = p_{g,R} \quad \| \quad p_{c,L,max} = p_{g,L} \qquad (c) \qquad (20)$$

When re-entering the gap after a new maximum displacement y_{max}, also the reactions associated with the gap spring components (drag and

separation) are re-initialised ($p_d = p_{sp} = 0$, $p_{c,max} = p_s = p_m$), where p_m is the reaction component in the memory element — this happens because an update of y_{max} alters the gap geometry and resets its constitutive description. As suggested from field data and discussed in Section 4.3, Eq. (19) implies that the average closure spring stiffness decreases with increasing $|y_{max}|$; this feature can be easily overridden by replacing y_{max} with $y_{g,0}$ in the denominator of the exponent in Eq. (19). From an implementation standpoint, it is worth noting that the updated value of $p_{c,max}$ can be lower than its value in a previous geometrical configuration of the gap (i.e., with different value of $|y_{max}|$).

Typical reaction–deflection responses resulting from the series combination of the closure spring and the soil element is shown in Fig. 6(b) for different values of the α_c and α_{sp} parameters and $\beta_{sp} = 10^5$. The formulation of the closure spring ensures that upon unloading from $p_c = p_{c,max}$, the closure spring reaches a nil asymptote ($p_c = 0$) as fast as enabled by the selected pair of $m_c - \alpha_c$ values, so as to reproduce the desired S-shape of the $p - y$ response. Ideally, the gap shape parameters should be identified against back-calculated cyclic $p - y$ curves from pile loading tests in soil exhibiting cohesive behaviour (e.g., due to unsaturated conditions). Values such as $m_c = 0.6$ and $\alpha_c = 20$ seem to provide a reasonable closure response for a sharp pile–soil separation, and can be henceforth considered as a first-guess parameter calibration.

3.1.3. Combined memory and drag springs

To properly capture cyclic pile–soil interaction in the presence of gapping, a $p - y$ model should also be able to reproduce the frictional
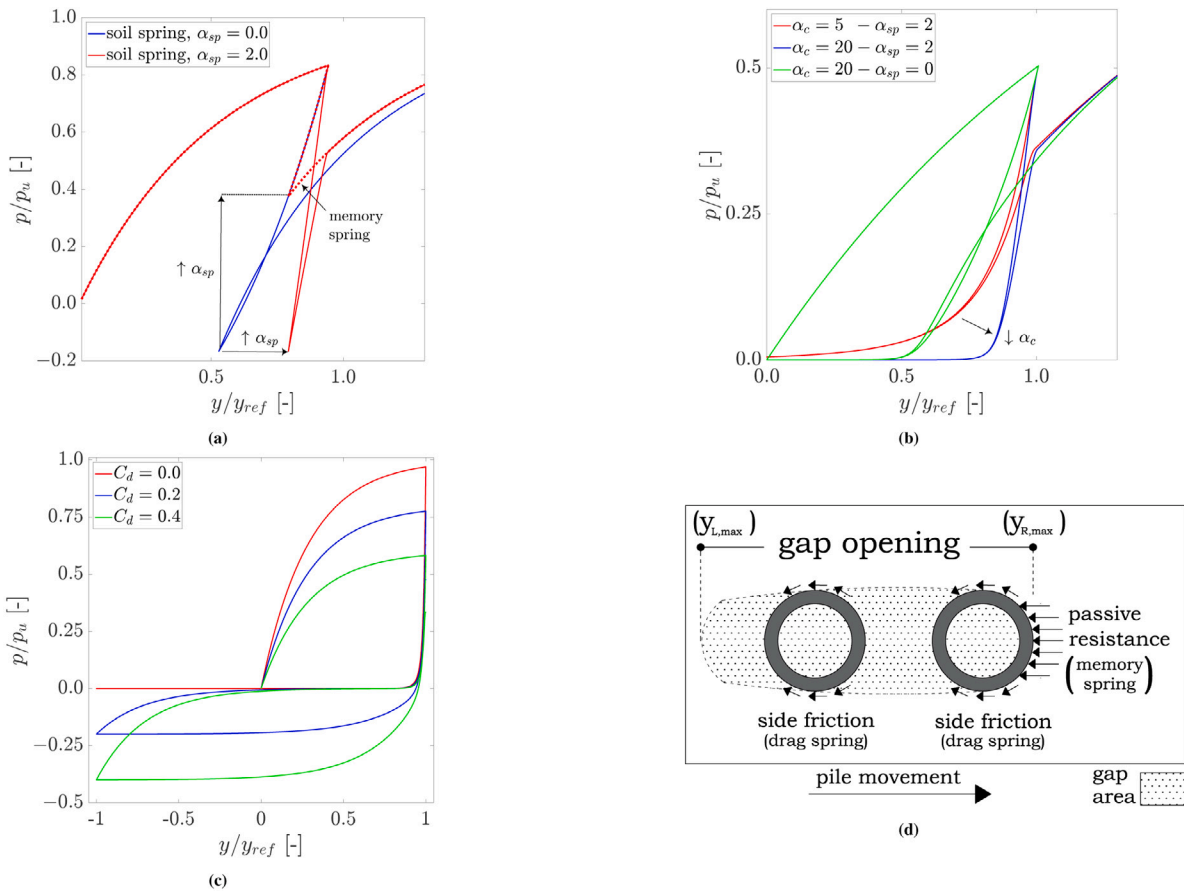
Fig. 6. Impact of (a) the separation spring, (b) the closure spring, and (c) the drag spring on the cyclic soil reactions in the presence of pile–soil gapping. Spring calibration settings in (a), (b), and (c) are same as reported in Fig. 2 unless mentioned otherwise. (a) shows the role of the separation spring — in parallel with the memory spring (Fig. 5). Solid and dotted lines denote the (global) soil and (individual) memory spring responses, respectively — note that for $\alpha_{sp} = 0$, the soil component reduces to the soil memory spring ($\mu_0 = 0$, $\beta_{sp} = 10^5$). Arrows (↑) highlight the impact of an increasing α_{sp} value on the soil spring response; (b) illustrates the role of the closure spring — in series with the soil spring (Fig. 5) for different values of α_c and α_{sp} ($m_c = 0.6$, $\mu_0 = 10$); (c) clarifies the influence of the C_d parameter on the gapping response of the $p - y$ model (either right or left component) under displacement-controlled cyclic loading ($\alpha_{sp} = 2$, $m_c = 0.6$, $\alpha_c = 20$, $\mu_0 = 10$); (d) depicts the soil resistance mechanisms against rightward motion (from $y_{L,max}$ to $y_{R,max}$) for a pile in unsaturated sand.

resistance offered by the side soil wall when normal contact is lost on one or both sides of the pile — see in Fig. 6(d) the relevant resisting mechanisms for a pile moving from $y_{L,max}$ towards $y_{R,max}$. Frictional drag (side pile–soil friction, introduced via the drag spring) resists pile motion regardless of the pile location and displacement direction within the gap area. Conversely, the passive soil resistance (from the memory spring) manifests itself only when the pile is acting to enlarge the gap – i.e., when the pile displacement y equals either $y_{L,max}$ (with $\dot{y} < 0$) or $y_{R,max}$ (with $\dot{y} > 0$). Frictional drag is incorporated in the proposed model by setting the closure spring in parallel with a drag spring, in a fashion similar to that proposed by Boulanger et al. (1998).

In light of the chosen setup of the separation and gap springs, the resulting gapping $p-y$ model (left + right sides) will respond to, e.g., a rightward monotonic load as follows:

1. The $p-y$ element on the right opposes the pile deflection through the memory spring exclusively ($y_{R,max} = y_{max}$) – in fact, no additional resistance is offered by the (deactivated) gap and separation springs when the pile and the soil are in contact;

2. On the left side, the soil reaction is almost completely provided by the drag spring, since the flexibility of the overall soil element (memory + separation springs) is nearly nil when the separation spring is active (for rightward monotonic loading, when $y_{L,max} = 0 < y$). Additionally, the closure spring is practically inactive under these conditions, since the associated reaction already lies on its nil asymptote ($p_{c,max} = 0$).

In conclusion, for monotonic loading, the set of soil reactions in the presence of a gap includes the memory and drag reactions on the 'passive' and 'active' sides, respectively — clearly, the attribute of passive or active side depends on the direction of the external lateral load.

A desirable feature of the overall $p - y$ formulation is to ensure perfect compatibility between the model responses obtained with and without gap modelling. Such compatibility is ultimately guaranteed by combining, when gapping is enabled, the following monotonic responses of the memory and drag springs, which is altogether equivalent to the original *SL* formulation — see Eq. (1):

$$p_d = p_{u,d} \left[1 - e^{-\alpha\left(|y_g - y_g^r|/D\right)^m} \right] \tag{21}$$

$$p_m = p_{u,m} \left[1 - e^{-\alpha|y_s/D|^m} \right] \tag{22}$$

where $p_{u,d} = C_d p_u$ and $p_{u,m} = (1 - C_d) p_u$, while $y_g^r = y_g$ is updated at every sign reversal of $\dot{y}_g$ (at the beginning of the analysis, the initialisation $y_g^r = y_g = 0$ is set). C_d is a scalar parameter that can be tuned between 0 and 1 to modulate the relative contribution of the drag reaction to the total lateral soil resistance. Since during monotonic rightward loading the two springs share the same displacement value (as discussed above, $y_{s,R} = y_{g,L} = y$), then Eq. (1) results exactly from the sum of the p_d and p_m reactions. The calibration of the drag and memory reaction parameters requires only the additional identification of C_d, since p_u, α, and m can be obtained through the CPT-based
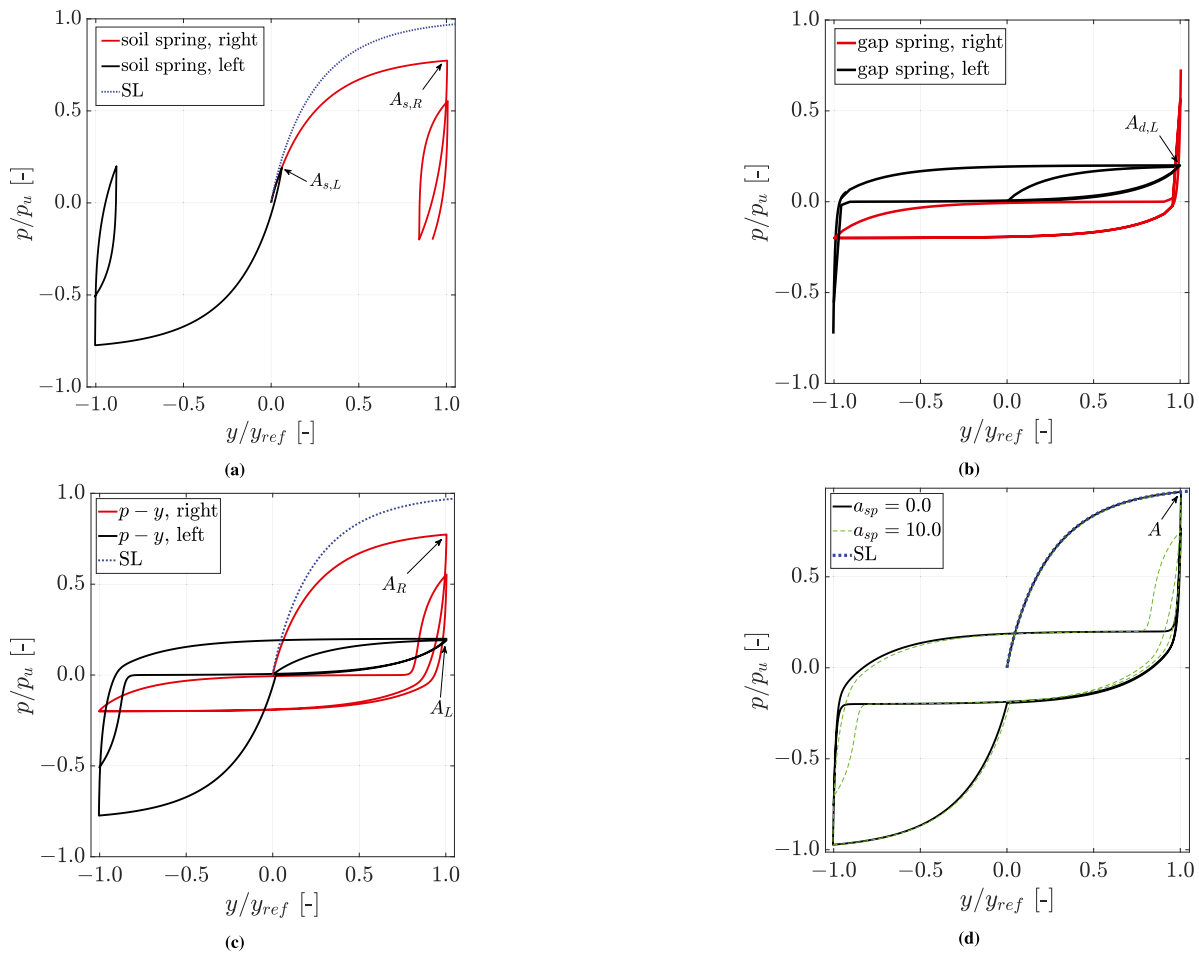
Fig. 7. Force–displacement response to $N = 2$ displacement-controlled cycles. The unsaturated $p - y$ spring is presented in (d) after its sub-components in (a), (b), and (c). Black and red colours denote the response of the L and R interaction elements in Fig. 5, while blue is used for the monotonic response of the overall $p - y$ spring with total capacity equal to p_u. In (d), the impact of the separation spring stiffness on the global response is shown in green. Points A denote the occurrence of the peak monotonic load in the global $p - y$ spring (d) and its sub-components (a–c). Relevant parameters are the same as reported for Fig. 2, along with: $C_d = 0.2$, $\alpha_c = 60$, $\alpha_{sp} = 0$, $\mu_0 = 10$).

procedure proposed by Suryasentana and Lehane (2016) (Eq. (2)). The impact of C_d on the response of the right/left spring component is illustrated in Fig. 6(c)

The implications of the above modelling assumptions are visualised in Fig. 7, which illustrates the response of the complete $p-y$ scheme in Fig. 5 to displacement-controlled two-way loading (with $N = 2$ loading cycles). Fig. 7(d) confirms that the monotonic response of the gapping $p - y$ model is coincident with the target SL formulation — see the performance of distinct model components in Figs. 7(a) and 7(b), where red/black solid lines and dots are used to illustrate the responses of the right/left soil and gap springs, respectively. When the maximum reaction value is achieved during the first monotonic loading branch (point A in Fig. 7(d)), the component from the right soil spring is at the level A_R (Fig. 7(c)), while the left drag and soil springs are at the levels $A_{d,L}$ and $A_{s,L}$, respectively. This outcome is in agreement with previous statements, i.e., no contribution from the right gap spring and left closure spring, plus minimal contribution from the left soil element. Finally, Fig. 7(c) displays the contributions of the left and right spring components, which provide altogether ($y_L = y_R = y$ and $p_L + p_R = p$, Table 1) the unsaturated $p - y$ response shown in Fig. 5.

After establishing suitable working principles for the memory and drag springs under monotonic loading, their extension to cyclic loading conditions is relatively straightforward. The cyclic response of the memory spring results from the evolution of the memory-enhanced hardening modulus in Eq. (15), according to the same bounding surface formulation described in Section 2 – the calibration of the ratcheting

control parameter μ_0 is likewise required. On the other hand, the desired cyclic response of the drag element is shown in Fig. 8 to exhibit some different features in comparison to the cyclic memory spring. The cyclic rules given below are applicable to both left and right drag springs, except for the signs of relevant inequalities ($<$ or $>$) (they are opposite on the two sides of the pile — for brevity, only the right drag spring is considered below). In Fig. 8, the cyclic response of a drag spring (right side of the pile) is displayed starting from a configuration with pile–soil contact ($y_g - y_g^r = 0$), then under cyclic loading within the gap ($y_g - y_g^r < 0$), – e.g., ($y_g - y_g^r > 0$) for the left spring component, and finally towards gap re-closure ($y_g - y_g^r = 0$). A requirement introduced by separately modelling the left and right sides of the pile is the need for the drag reaction to precisely meet the values $p_d = 0$ and $y_g - y_g^r = 0$ upon complete re-closure – i.e., upon pile–soil contact the drag spring (on the contact side) does not oppose any resistance, while the closure spring resists with $p_c = p_{c,max}$. The described drag reaction mechanism (right spring component) can therefore be calculated according to the following possible cases:

- $\dot{y}_g < 0$, i.e., pile moving along the gap-opening path ($r_1 \rightarrow r_2$ in Fig. 8);
- $\dot{y}_g > 0$, i.e., pile re-closing the gap (towards the origin ($y_g - y_g^r \rightarrow 0$)
  - $r_2 \rightarrow r_3$, $r_4 \rightarrow r_0$);
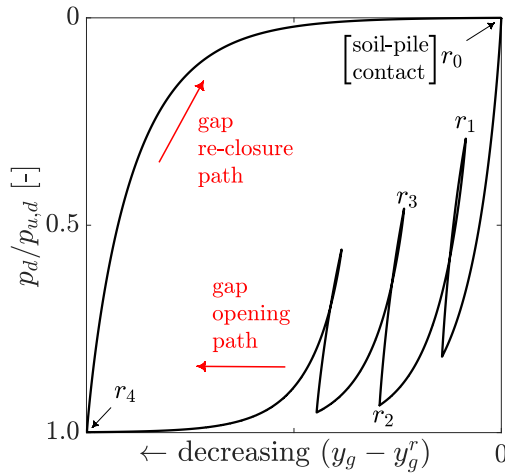- $\dot{y}_g = 0$, no force increment.

Fig. 8. Response of the right drag spring component (for the left drag spring $y_g - y_g^r$ would also be zero upon pile–soil contact, though increasing towards the inner part of the gap) to cyclic loading — all relevant parameters (m, α, D) set as for Fig. 2.

$$p_d = \begin{cases} (\dot{y}_g < 0) & (a) \\ p_d^r + \text{sgn}(\dot{y}_g) \cdot \left[p_{u,d} - |p_d^r| \right] \left[1 - e^{-\alpha \left| (y_g - y_g^r)/D \right|^m} \right] & \\ (\dot{y}_g > 0) & (b) \\ p_d^r + \text{sgn}(\dot{y}_g) \cdot p_{u,d} \left[1 - e^{\alpha_d^r \left| (y_g - y_g^r)/D \right|^m} \right] & \\ (\dot{y}_g = 0) & (c) \\ p_d & \end{cases} \qquad (23)$$

in which the internal variables p_d^r and y_g^r, represent the drag reaction and displacement at the last load reversal. Entering the gap from $y = y_{max}$ resets p_d^r and $y_g - y_g^r$ to zero (i.e., $y_g^r = y_g$). For $\dot{y}_g < 0$, the shape parameter α is replaced by α_d^r (< 0) as,

$$\alpha_d^r = \frac{\ln \left(1 - |p_d^r|/p_{u,d} \right)}{(|y_g^r|/D)^m} \qquad (24)$$

which is updated when the displacement direction changes from $\dot{y}_g > 0$ to $\dot{y}_g < 0$ (i.e., instances r_2, r_4 in Fig. 8), following the simple procedure described in Appendix B to ensure that a nil drag reaction results (i.e., $p_d = 0$) when $(y_g - y_g^r) = 0$. This choice determines the specific path from r_4 to r_0 in Fig. 8 – particularly, the use of α_d^r ensures that the drag spring is perfectly re-closed when the r_0 point is achieved).

3.2. From gapping $p - y$ modelling to cyclic pile response

The cyclic performance of the complete gapping $p - y$ model is exemplified in Figs. 9 and 10 with reference to force-controlled two-way and one-way cyclic loading, respectively. For the former case, the impact of the drag spring capacity is explored by setting $C_d = 0.1$ (Figs. 9a-b-c) and $C_d = 0.25$ (Fig. 9d-e-f), while all other parameters are identical regardless of C_d. Evidently, the particular repartition of the identical ultimate capacity (at the level of the whole gapping $p - y$ model) over the memory and the drag springs has a significant impact on the observed global response, particularly on the displacement accumulation behaviour (Figs. 9c–9f) – $p_{u,m} = 0.9 p_u$, $p_{u,d} = 0.1 p_u$ in Fig. 9c, and $p_{u,m} = 0.75 p_u$, $p_{u,d} = 0.25 p_u$ in Fig. 9f. It is expected that larger drag resistance should result in less displacement accumulation, since the work of the applied loads will be increasingly spent against the pile–soil drag resistance, rather than to enlarge the gap opening.

The model naturally captures this aspect through the influence of the drag coefficient C_d – in essence, a capacity repartition parameter — on the stress paths within the soil and gap springs.

For the case of one-way cyclic loading, the gapping $p - y$ response is illustrated in Fig. 10, which displays the outcome of combining all the modelling features for gapping and ratcheting control described above. In Fig. 10a the response of the soil springs can be observed (the separation springs are deactivated by setting $\alpha_{sp} = 0$, so that the soil springs reduce to the sole memory springs). In the same figure, a small contribution of the memory spring is shown for the left side of the pile, which would further decrease for larger α_{sp} values — cf. to Eq. (18). As a next step, Fig. 10b illustrate the response of the global left and right $p - y$ springs: on the left side, the observed deformation is to be mainly attributed to the drag spring, since (i) the deformability of the soil spring is limited (cf. to Fig. 10a), and (ii) within the gap spring, the closure spring opposes no resistance as $p_{c,L,max} = 0$. Finally, the global response of the whole gapping $p - y$ spring is depicted in Fig. 10c.

The response to lateral cyclic loading of the tubular steel pile in Fig. 11(a) was simulated through a 1D FE model endowed with the complete gapping $p - y$ model described in this section. The FE model set-up is identical to that presented in Section 2.3 (Fig. 3(a)) and, similarly, the assumed soil profile features a linearly increasing cone resistance $q_c = 5 + 2z$ [MPa] with a uniform distribution of the ratcheting parameter $\mu = 20$ along the depth z. The following additional parameters values were chosen to complete the calibration of the gapping $p - y$ model: $C_d = 0.1$, $\alpha_{sp} = 0$, $m_c = 0.5$, $\alpha_c = 10$. The transition from unsaturated to saturated soil conditions (i.e., location of the water table) was arbitrarily set at $z = 4$ m, and therefore gapping $p-y$ springs (on both sides of the pile) and non-gapping memory springs (on one side only) were distributed over the depth intervals $z = 0-4$ m and $z = 4-8$ m, respectively. The resulting pile response is shown in Fig. 11. The impact of the unsaturated zone on the lateral pile response (especially under 2-way loading) is very evident — cf. to Figs. 11 and 3(c)). The calculated 1-way response compares well (qualitatively) with the field data presented in Kementzetzidis et al. (2022), and captures the data discussed in Section 4 for the reference impact-driven pile. For 2-way loading, the calculated response in Fig. 11(c) can reproduce the global S-shaped response loops that are observed for piles in cohesive soils, and is largely consistent with the general experimental observations of Suzuki and Nakai (1985). In this regard, it is also worth noting that the tangent stiffness associated with the pile head response tends to increase under cycling during stages of pile–soil contact as consequence of the ratcheting control mechanism, while the occurrence of gapping – and the gradual enlargement of the gap size – determine a reduction of the average (or secant) stiffness.

4. Comparison to field measurements

In this section, the performance of the proposed $p - y$ formulation is evaluated against the results of a lateral pile loading field test performed on a 10m-long tubular steel pile — see all geometrical specifications in Table 3. The field measurements considered herein were recorded during the experimental campaign associated with the Gentle Driving of Piles (GDP) project (Metrikine et al., 2020), which too place at the sandy Maasvlakte II site at the port of Rotterdam. The reference pile was impact hammered on November 4 2019 down to a target depth of 8 m, and then laterally loaded on December 9 with an eccentricity $e = 1$ m above the ground surface. The lateral loading test was performed using a custom-built load frame in combination with a larger/stiffer reaction pile. The pile was instrumented with fibre Bragg grating (FBG) sensors at multiple locations, which enabled to obtain the bending moment profiles discussed later on. Further details regarding pile instrumentation, loading equipment, and test setup are provided by Tsetas et al. (2022) and Kementzetzidis et al. (2022). Prior to pile installation, a comprehensive site investigation was carried out (Tsetas et al., 2022), including borehole sampling and Seismic CPTu
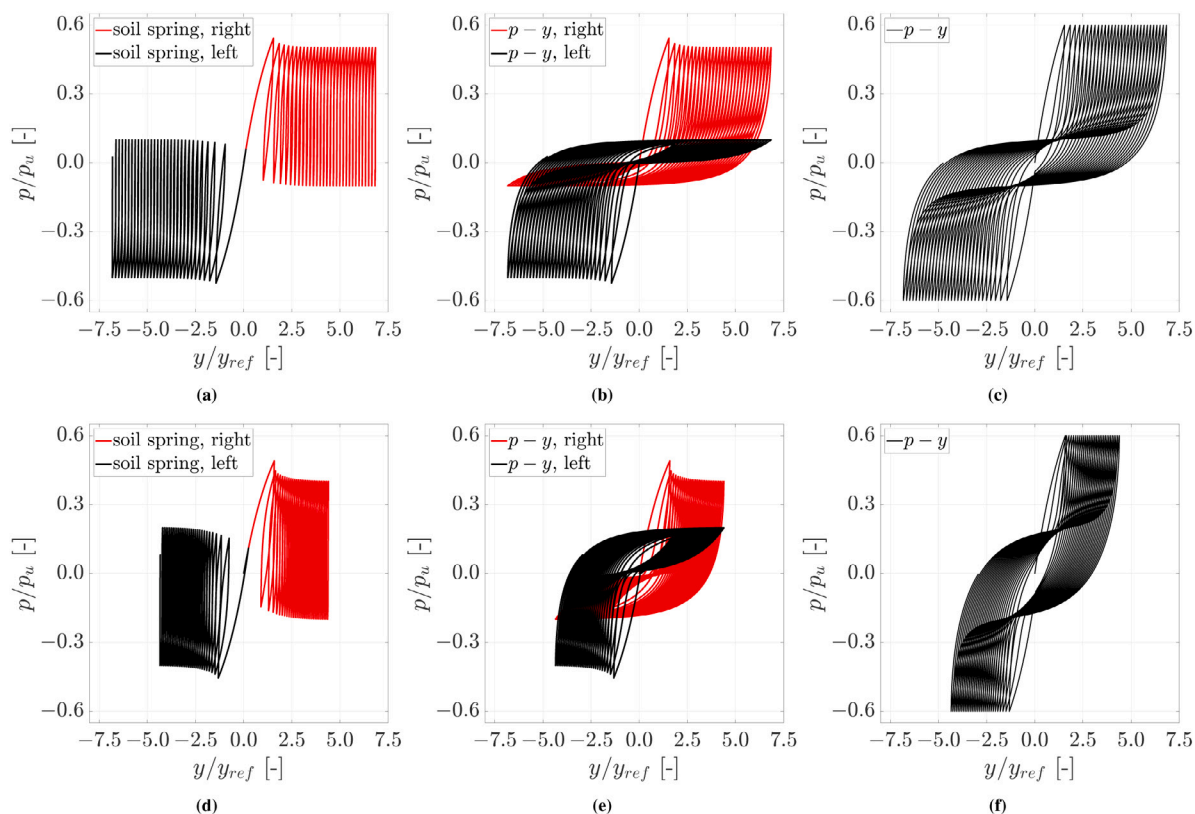
Fig. 9. Force–displacement response to $N = 30$ force-controlled two-way cycles for (a-b-c) $C_d = 0.1$ and (d-e-f) $C_d = 0.25$. For both cases, the global $p - y$ response is presented in (c) and (f) after the soil sub-components (soil springs) in (a) and (d), and the global left and right components in (b) and (e). Black and red colours denote the responses of the left and right interaction elements in Fig. 5. Relevant model parameters are the same as reported for Fig. 2, along with: $C_d = 0.1/0.25$, $\alpha_{sp} = 0$, $\alpha_c = 5$, $m_c = 0.6$, $\mu_0 = 20$).
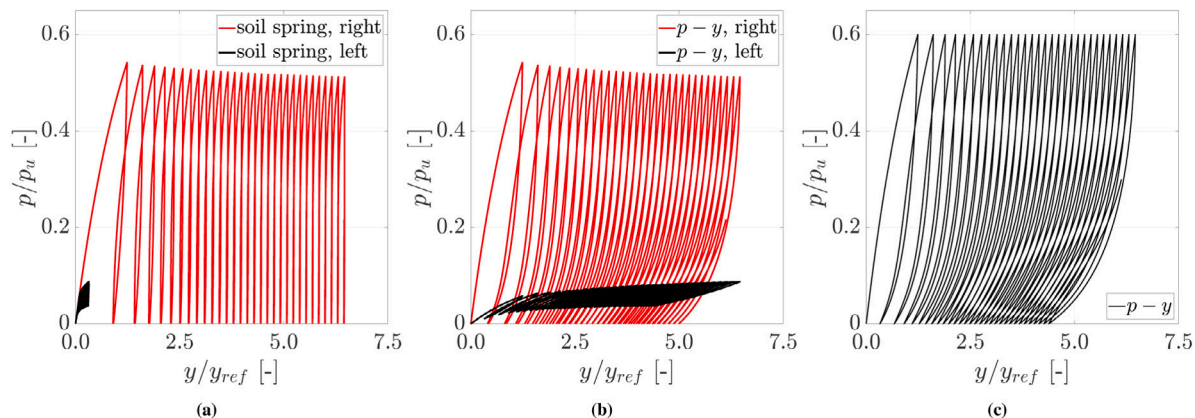

Fig. 10. Force–displacement response to $N = 30$ force-controlled one-way cycles. The global $p - y$ response is presented in (c) after the soil sub-components (soil springs) in (a), and the global left and right components in (b). Black and red colours denote the responses of the left and right interaction elements in Fig. 5. Relevant model parameters are the same as reported for Fig. 2, along with: $C_d = 0.1$, $\alpha_{sp} = 0$, $\alpha_c = 5$, $m_c = 0.6$, $\mu_0 = 50$).

(SCPTu) tests (target depth: 10 m). The soil deposit was found to mainly comprise medium-dense to very dense sand ($D_r = 60 - 100\%$ – with an overall negative D_r depth-gradient), with a water table located about 4 m below the ground surface. Profiles at the reference pile location of cone resistance (q_c) and soil's relative density (D_r) (obtained based on Jamiolkowski et al., 2003) are shown in Fig. 12(a).

4.1. Cyclic/dynamic lateral loading programme

The reference pile was subjected to the cyclic/dynamic loading programme illustrated in Fig. 12(b), which lasted approximately 40 h and featured a total amount of loading cycles equal to $N = 82000$.

Table 3
Geometrical specifications for the reference test pile.

		Test piles	Reaction pile
Total length	L	10 m	10 m
Embedded length	L_e	8 m	8 m
Outer diameter	D	0.762 m	1.6 m
Wall thickness	h	1.59 cm	2 cm

Some of the cycles were applied with relatively large amplitude at constant/low frequency (black parcels in Fig. 12(b)), with interleaved stages of small-amplitude loading at variable frequency (henceforth
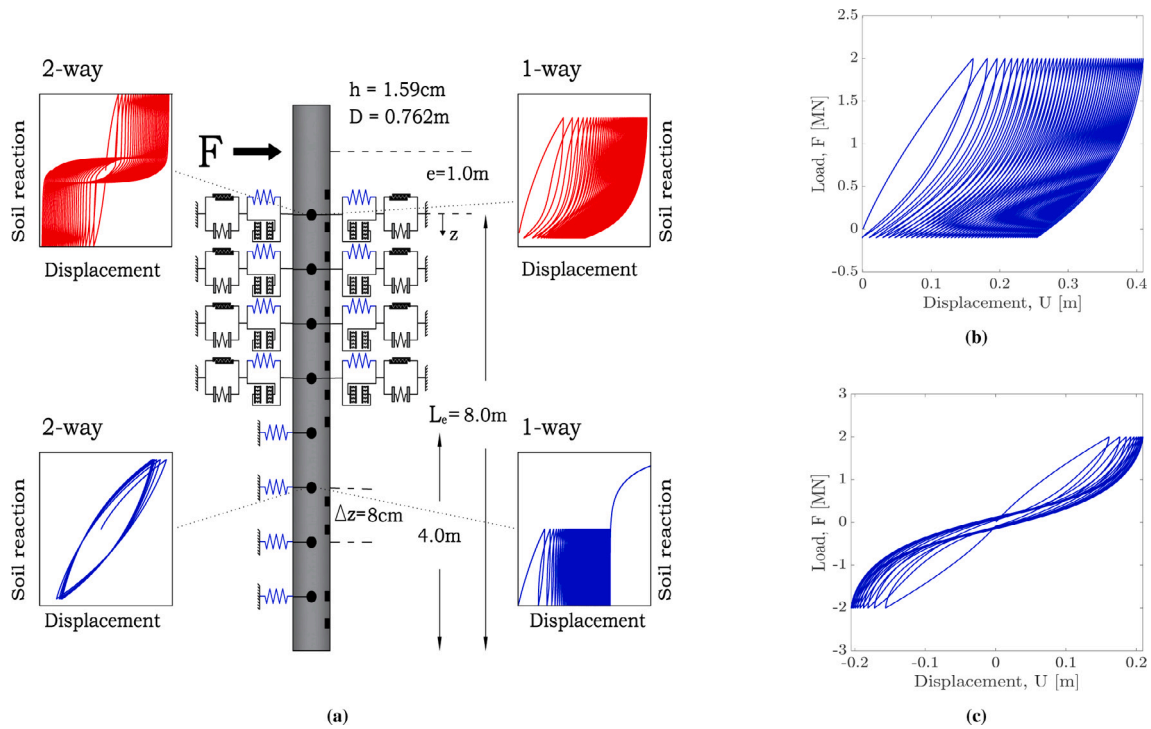
Fig. 11. (a) Reference pile subjected to lateral cyclic loading: typical one-way vs two-way response of the soil reaction springs in agreement with the proposed gapping $p - y$ formulation with ratcheting control. The black rectangular symbols indicate the locations of the FBG sensors mentioned in Section 4. Simulated load–displacement pile response at ground surface to (b) one-way and (c) two-way cyclic loading ($N = 50$ loading cycles) for the reference pile in (a).

Table 4
Loading specifications for the cyclic/dynamic field tests — cf. to Fig. 12(b), Eq. (25).

–	F_{av} [kN]	F_{cyc} [kN]	f [Hz]	$N \times 10^3$	–	F_{av} [kN]	F_{cyc} [kN]	f [Hz]	$N \times 10^3$
$0_{7.5}$	7.5	2.5	0.1–4	4.8	c_{90}	89.5	2.5	0.1–4	4.8
a	**90**	**85**	**0.1**	**1**	$c_{7.5}$	7.5	2.5	0.1–4	4.8
a_{90}	89.5	2.5	0.1–4	4.8	d	**90**	**85**	**0.1**	**1**
$a_{7.5}$	7.5	2.5	0.1–4	4.8	d_{178}	177.5	2.5	0.1–4	4.8
b	**177.5**	**172.5**	**0.1**	**1**	d_{90}	89.5	2.5	0.1–4	4.8
b_{178}	177.5	2.5	0.1–4	4.8	$d_{7.5}$	7.5	2.5	0.1–4	4.8
b_{90}	89.5	2.5	0.1–4	4.8	e	**177.5**	**172.5**	**0.1**	**1**
$b_{7.5}$	7.5	2.5	0.1–4	4.8	e_{178}	177.5	2.5	0.1–4	4.8
b_{220}	219.5	2.5	0.1–4	4.8	e_{90}	89.5	2.5	0.1–4	4.8
c	**220**	**130**	**0.1**	**1**	$e_{7.5}$	7.5	2.5	0.1–4	4.8
c_{220}	219.5	2.5	0.1–4	4.8					

Table 5
Technical specifications of FBG strain sensors.

Type	Sylex FFA-01
Number of sensors	24 (12 per side)
Measurement range	±3000 µm/m
Wavelength range	1510 nm – 1590 nm

4.2. Impact of unsaturated soil conditions on cyclic pile response

Due to the frequent rainfalls in the Rotterdam area, the shallowest soil at the Maasvlakte II site was unsaturated, which had a clear impact on the recorded pile response in that it enabled pile–soil gapping under cyclic loading. In a related study, Kementzetzidis et al. (2022) inferred a maximum gap depth of approximately 4 m (i.e, as deep as the water table) by examining the measured bending moment profiles. Qualitatively, the experimental one-way cyclic response of the test pile in Fig. 13(a) recalls the simulated cyclic behaviour of a pile supported by the proposed gapping $p - y$ model — cf. to Fig. 11, but note that the $p - y$ parameters initially assumed in Section 3.2 are not representative of the specific soil conditions at the Maasvlakte II site. In both cases, the tangent stiffness (K_{tang}) is severely affected by the distance to the maximum lateral displacement ever experienced (which is an approximate measure of the gap opening), as typically observed for cyclically loaded piles in the presence of a gap.

Additional light into the field response of the pile can be shed by analysing the lateral soil reactions back-calculated from axial strain measurements). Axial strains were measured via fibre Bragg grating (FBG) sensors – in-line and rosettes, installed at 13 different cross sections along the pile length (see specifications and locations in Tables 5–6); at each depth, two sensors were installed at diametrically opposite locations on the external pile surface.

For slender piles, lateral $p - y$ reactions can be derived based on the standard Euler–Bernoulli beam theory — measured axial strains (ϵ_{zz}) can directly be converted into profiles of beam curvature and bending

referred to as dynamic 'frequency sweeps' or 'f-sweeps' – grey parcels in Fig. 12(b)). Each load parcel was defined by superimposing a monoharmonic excitation of amplitude F_{cyc} and frequency f onto an average load level F_{av}:

$$F(t) = F_{av} + F_{cyc} \times \sin(2\pi f t) \tag{25}$$

In particular, each low-frequency cyclic parcel ($a - e$ in Fig. 12(b)) comprised $N = 1000$ cycles; the 16 f-sweeps featured $N = 4800$ cycles applied at a constant/low amplitude of $F_{cyc} = 2.5$ kN, while the loading frequency was increased from 0.1 Hz to 4 Hz with increments of 0.1 Hz every 120 cycles. All the loading settings associated with Eq. (25) and Fig. 12(b) are summarised in Table 4. All lateral loading parcels were applied with $F_{av} > F_{cyc}$, which corresponds with so-called 'one-way' loading (i.e., with no load sign reversals). The remainder of this work will focus on lateral pile–soil interaction under relatively large loading cycles (parcels $a - e$ in Fig. 12(b)), assuming that the impact of small-amplitude vibrations on the lateral ratcheting and gapping of the pile may be disregarded as shown in Kementzetzidis et al. (2022).
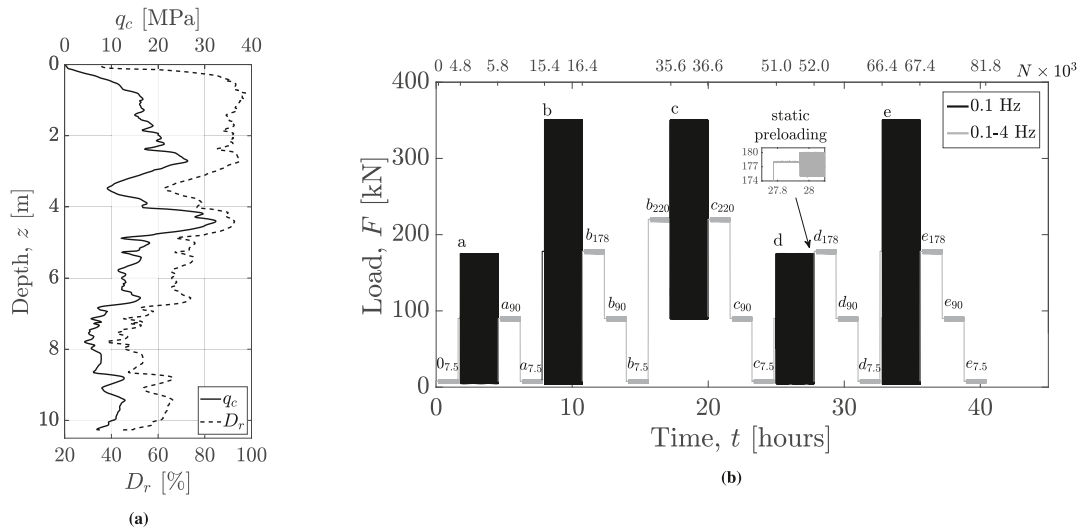
Fig. 12. Profiles of cone resistance (q_c) and relative density (D_r) at the pile location in (a), and in (b) cyclic/dynamic loading programme. Load amplitudes are provided against time (bottom axis) and number of cycles (top axis). Cyclic load parcels ($a - e$, 1000 cycles per parcel) and dynamic f-sweeps ($a - e_{7.5,...,220}$, 4800 cycles per sweep) are shown in black and grey, respectively — see loading specifications in Table 4.

Table 6
FBG sensor locations along the pile length — cf. to Fig. 11(a). Except for the sensor installed at $z = -0.37$ m (rosette type), all sensors are of an in-line type.

	−0.37	0.23	0.77	1.30	1.78
z [m]	2.25	2.77	3.30	3.80	5.26
	5.77	7.00	7.50		

moment (M), which can then be used to obtain the evolution in time of the distributed soil reaction (p) and the corresponding pile deflection (y) at a certain depth. In the absence of inertial effects and axial loads, the following governing relationships hold:

$$M(z,t) = -EI \frac{\epsilon_{zz}(z,t)}{D/2} \qquad (26)$$

$$p(z,t) = -\frac{\partial^2 M(z,t)}{\partial z^2} \qquad (27)$$

$$y(z,t) = -\iint_L \frac{M(z,t)}{EI} \, \mathrm{d}z \, \mathrm{d}z \qquad (28)$$

where EI represents the flexural rigidity of the pile, $D/2$ is the distance of the FBG strain sensors from the neutral axis of the beam cross-section, and $p(z,t)$ is the soil reaction. For piles of low L/D ratio, such as that under consideration, the Timoshenko beam theory is known to be more suitable (Timoshenko, 1921) in that it considers the influence of shear deformations. Accordingly, the following set of differential equations may be considered for a pile of uniform flexural (EI) and shear (GA) rigidities:

$$\frac{M(z,t)}{EI} = -\frac{\epsilon_{zz}(z,t)}{D/2} = -\frac{\partial \phi(z,t)}{\partial z} \qquad (29)$$

$$p(z,t) = EI \frac{\partial^3 \phi(z,t)}{\partial z^3} \qquad (30)$$

$$\frac{\partial y(z,t)}{\partial z} = \phi(z,t) - \frac{EI}{\kappa GA} \frac{\partial^2 \phi(z,t)}{\partial z^2} \qquad (31)$$

where ϕ is the local rotation angle of a given cross-section, and κ a section-specific shear deformation factor – $\kappa = 0.57$ for the thin-walled circular cross-section of the pile at hand (Table 3 Hutchinson, 2001). The following procedure was adopted to estimate local reaction–deflection responses at arbitrary pile locations, using a finite number of strain measurements along the pile and polynomial fitting of moment profiles:

1. Profiles of lateral soil pressure were obtained via double differentiation (Eq. (30)) of the bending moment profiles (Eq. (29)). A low-order (3rd) polynomial function was adopted for fitting purposes, so as to avoid difficulties associated with the differentiation of higher-order polynomials;

2. The slope of the deformed pile axis, $\frac{\partial y(z,t)}{\partial z}$, was calculated via Eq. (31). At this point, a higher-order (fifth) polynomial was used to re-fit the moment profiles, which were then integrated to obtain $\phi(z,t)$ (Eq. (29)). The necessary integration constant was determined for each loading step by solving an algebraic equation for $\phi(z_0,t)$ (Eq. (31)), which requires the measurement of the beam axis slope at a chosen location $z = z_0$, as well as the value of $\frac{\partial^2 \phi(z_0,t)}{\partial z^2}$ (obtained via the previous step);

3. Finally, soil displacement profiles were obtained by integrating $\frac{\partial y(z,t)}{\partial z}$, with the relevant integration constant obtained by enforcing the measured value of lateral displacement at the ground level.

The strain gauge configuration with a relatively wide spacing of 70 cm approximately constant along the pile, Tsetas et al. (2022), see Table 6 and Fig. 11(a)) rendered the $p - y$ curve identification process quantitatively sensitive to the order of the polynomial fitting functions. Nevertheless, the qualitative features of the back-calculated $p-y$ curves are relatively unaltered by the specific interpolation choices, and are exemplified in Fig. 14 for a pile location at a depth $z = 0.8$ m and the first 100 cycles of the loading parcel a in Fig. 12(b).

4.3. 1D modelling of cyclic pile response

The cyclic field response of the reference impact-driven pile was numerically simulated via the same 1D FE model illustrated in Fig. 11(a) (previously set up in view of this final simulation exercise). Gapping $p - y$ springs were distributed along the pile from ground surface ($z = 0$ m) down to the estimated depth of the phreatic level ($z = 4$ m), while only memory springs (Section 2) were applied to the lower portion of the pile in saturated sand ($z = 4 - 8$ m). An inter-spring spacing of 0.08 m was found appropriate to capture the cone resistance profile in Fig. 12(a), as well as to accurately solve the 1D boundary value problem at hand. Since what follows focuses on the pile response to the cyclic/low-frequency parcels in Fig. 12(b) (from a to e), inertial effects were deemed negligible. It should also be noted that no additional soil reaction mechanisms were considered in this 1D modelling study, such
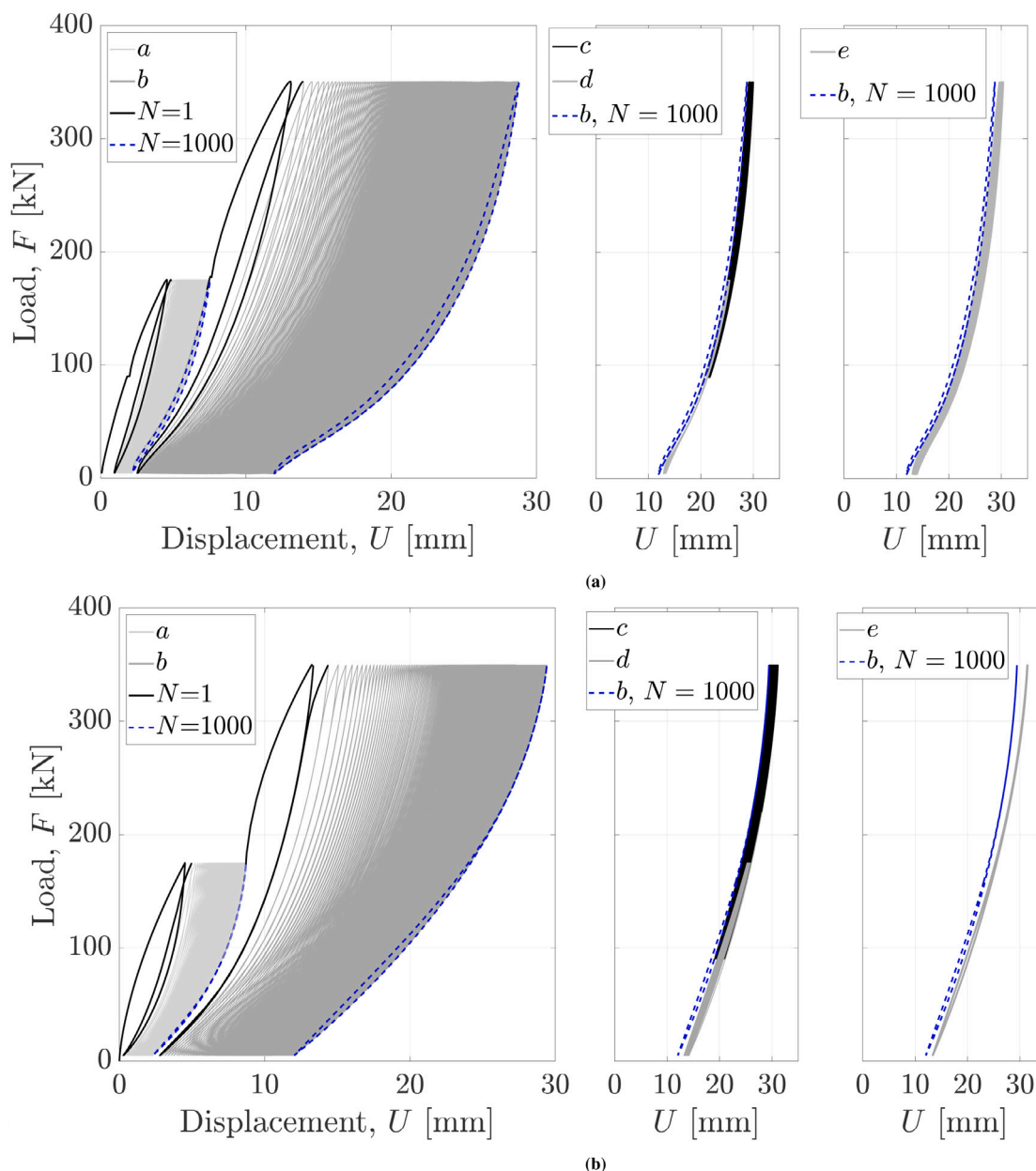
Fig. 13. Measured (a) and simulated (b) force–displacement pile response at ground level to the load parcels $a - b$ (left), $c - d$ (middle), and e (right) associated with lateral loading programme in Table 4. On the left, the solid black and dashed blue lines denote $N = 1$ and $N = 1000$, respectively; in the middle and right subfigures, the dashed blue lines indicate $N = 1000$ for parcel b.

as distributed moment reactions associated with shear stresses along the pile shaft, and/or shear resistance and moment fixity at the pile base — cf. to the PISA method proposed for large-diameter offshore monopiles (Byrne et al., 2019; Burd et al., 2020). Such a choice was justified by (i) the relatively small diameter of the pile ($D = 0.762$ m), (ii) its aspect ratio at the transition between flexible and rigid pile behaviour, and (iii) the lack of fully reliable $q_c \rightarrow D_r$ correlations for the high relative density characterising the shallowest sand layers at the Maasvlakte site (Fig. 12(a), Kementzetzidis et al., 2022) – this factor would have added further uncertainty to the calibration of additional soil reaction mechanisms using the D_r-based PISA correlations (Burd et al., 2020).

To simulate the cyclic response of the reference test pile, all $p - y$ model parameters must be first calibrated. Although $p - y$ reaction curves back-calculated from measured strain data could ideally have supported such endeavour, the abovementioned uncertainties in the

interpolation of moment profiles discouraged the use of strain data for quantitative parameter calibration.

An initial calibration trial was conducted by applying the CPT-based procedure by Suryasentana and Lehane (2016) (Eq. (2)[†]) to the first monotonic pile response branch associated with parcel a in Fig. 12(b) – i.e., with the lateral load F ranging from 0 to 175 kN. Using the suggested calibration procedure, both $p - y$ (for saturated sand) and memory springs were calibrated (only p_u, α, and m impact the monotonic pile response — also for the gapping $p - y$ springs) prior to subjecting the pile to lateral monotonic loading. The measured pile deflection response (black line) and the corresponding moment

---

[†] Soil stresses determined using $\gamma_{sat} = 19.3$ kN/m³ and $\gamma_{unsat} = 15.2$ kN/m³ for, respectively, the saturated and unsaturated unit weight of the soil — values representative of $D_r = 70\%$ were obtained from lab tests results reported in Tsetas et al. (2022).
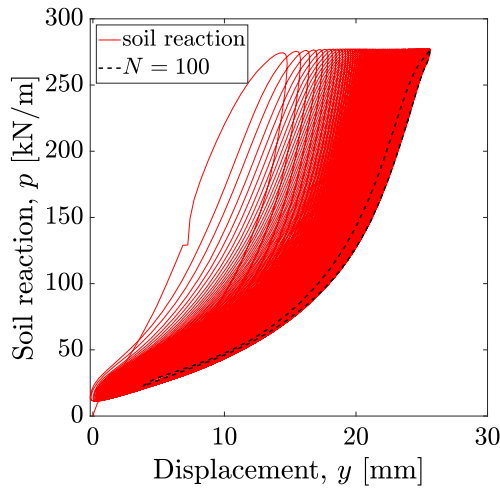
Fig. 14. Back-calculated soil reaction at depth $z = 0.8$ m for the first $N = 100$ cycles of the loading parcel a in Fig. 12(b).

profiles (black markers) at $F = 90$, 175 kN are compared in Fig. 15 to the 1D simulation results based on the SL calibration procedure (red lines). While the simulated moment profiles are rather satisfactory, a prominent under-prediction of the lateral pile stiffness was obtained — due to using the SL calibration method outside the recommended range of applicability and, potentially, to disregarding other soil resistance contributions in addition to normal $p - y$ reactions. The measured pile deflection at ground surface equals $U = 4.45$ mm (i.e, $U/D = 5.8 \cdot 10^{-3}$) when $F = 175$ kN, which is approximately half the minimum working threshold of $U/D \geq 10^{-2}$ ($U \geq 7.85$ mm) suggested by Suryasentana and Lehane (2016) for monotonic loading up to ultimate capacity — indeed, the GDP loading programme was conceived to investigate the pile response to medium–low amplitude loading cycles. The poor agreement between field data and SL-based simulations motivated a re-calibration of the proposed $p - y$ model that led to fully satisfactory results — see blue lines in Fig. 15. In particular, the following calibration guidelines were followed:

1. Regarding the calibration of the memory spring (both in saturated and saturated soil), the shape parameter m ($m = 0.5$ instead of 1.0) and the q_c-dependence of p_u in Eq. (2) was slightly modified (see Table 2) to best-fit the global lateral (monotonic) response of the pile as measured in the field (Fig. 15);

2. The calibration of ratcheting (μ_0) and gap-related parameters was solely based on parcels a and b (initial 2000 cycles of high amplitude loading), with no further adjustments for parcels $c - d - e$ (3000 cycles in total);

3. Due to the dearth of detailed data for calibration, the complexity of the calibration procedure was herein reduced by setting $\alpha_{sp} = 0$ (Eq. (18)) and $C_d = 0$ (Eq. (21)), and therefore deactivating the separation and drag springs;

4. Relevant shape parameters (m for the memory spring, m_c and α_c for the closure spring), were calibrated to match the global response of the pile upon unloading–reloading cycles. With reference to the closure spring, the global force–displacement response (Fig. 13(a)) and the back-calculated $p - y$ reaction trends (Fig. 14) generally suggested a gradual decrease in average soil reaction stiffness upon increasing pile deflection (Kementzetzidis et al., 2022). This aspect was accommodated by setting $\alpha_c = -\frac{\ln(0.15)}{(0.55)^{m_c=0.5}}$ – the reason for this setting is explained in Appendix B;

5. The ratcheting-control parameter μ_0 was identified against the displacement accumulation trends measured at the ground surface, under the simplifying assumption of negligible influence of

the degree of saturation (typically unknown and variable along the depth).

Regarding point 2, the deactivation of the separation and drag elements – which would in principle contribute to the flexibility of the $p - y$ model – was enforced in light of the following arguments:

– inhibiting the separation spring did not hinder the attainment of the sharp unloading stiffness, as it is anyhow achieved owing to the progressive stiffening of the memory spring (see also the previous discussion in Section 3.1.1);

– the qualitative shape of the back-calculated soil reactions (Fig. 14) indicated very weak influence of pile–soil drag, partly due to the one-way cyclic loading considered herein (the contribution of soil drag would be higher under two-way loading with load sign reversals).

As for the calibration of μ_0, it is well-reported in the literature that the accumulation of soil strains associated with cyclic ratcheting is substantially affected by the initial mean effective stress $\bar{\sigma}_0'$ – namely, lower $\bar{\sigma}_0'$ leads to higher/faster strain accumulation (Wichtmann et al., 2005). To heuristically incorporate this notion into the calibrated $p - y$ model, the following calibration relationship was introduced for μ_0:

$$\mu_0 = \mu_c \cdot e^{C_p \cdot \left(\frac{\bar{\sigma}_0'}{\bar{\sigma}_{ref}} - 1 \right)} \tag{32}$$

where C_p and μ_c are scalar factors to be identified, while $\bar{\sigma}_{ref} = 100$ kPa is a reference pressure. Eq. (32) implies a depth-dependence of μ_0 through the in-situ $\bar{\sigma}_0'$ profile (calculated using an at-rest earth pressure coefficient equal to 0.5, and $\gamma_{sat} = 19.3$ kN/m³ – $\gamma_{unsat} = 15.2$ kN/m³), though with no attempt of capturing further expected dependencies on the pile geometry and the features of the cyclic loading programme (Wichtmann et al., 2005) – such dependencies are implicitly included in the selected values of C_p and μ_c, and would require additional studies to be deciphered in detail. While such studies were beyond the scope of this work, the whole set of $p - y$ parameters identified to reproduce the response of the reference test pile are reported in Table 2.

4.4. 1D simulation results

Following the set-up of the 1D FE pile model (Fig. 11(a)) and the calibration of all $p - y$ parameters (Table 2), the response of the reference test pile to the cyclic load parcels $a - e$ in Fig. 12(b) was numerically simulated. The comparison between measured and computed force–displacement responses (displacement recorded at the ground surface) is shown in Fig. 13, while the corresponding displacement accumulation trends (ground level displacement vs number of loading cycles) are compared in Fig. 16. Finally, simulated and measured bending moment profiles are reported in Fig. 17 for six different times along the cyclic loading history.

Considering the lack of data for direct calibration (i.e., reliable $p - y$ curves obtained pile strain measurements), the global response of the pile seems to be overall well-captured by the model in several respects. With particular regard to the force–displacement loops in Fig. 13, it may be stated that:

– the response to the initial monotonic branches in the cyclic parcels a ($F = 0 - 175$ kN) and b ($F = 175 - 350$ kN) are very well-captured;

– the softening in the unloading–reloading response measured in the field, (compare $N = 1$ to $N = 1000$ for parcel b in Figs. 13(a) and 13(b)) is also adequately captured owing to the gapping modelling features described above;

– cyclic hysteresis (area of force–displacement loops) is mostly well-reproduced, with the exception of the first few cycles of parcel b. Further improvement in this respect could be achieved, for instance, by activating/calibrating the dragging mechanism (here inhibited for simplicity).
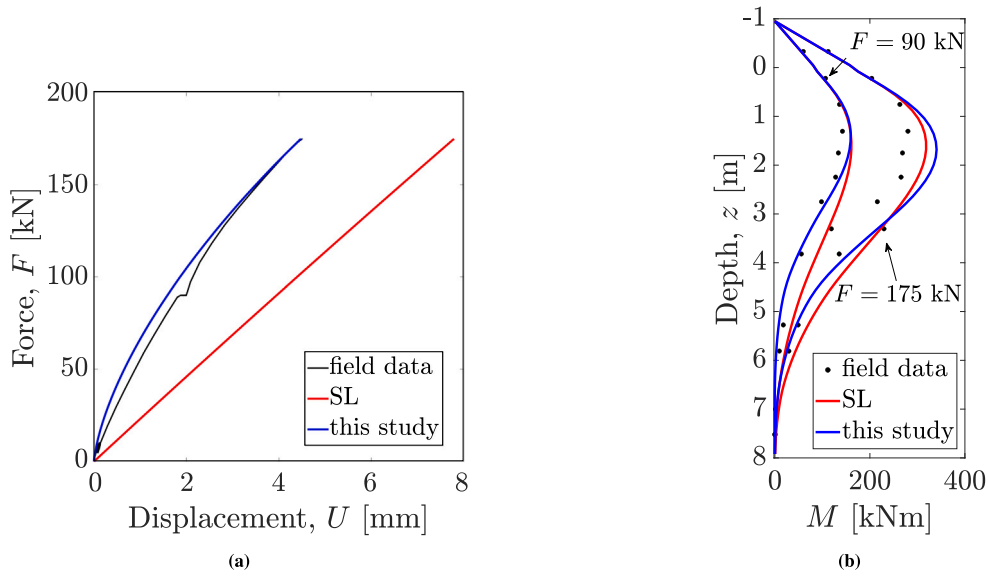
Fig. 15. Comparison between simulated and measured pile response to the first monotonic loading branch associated with parcel *a* in Fig. 12(b): (a) force–displacement response at ground surface, and (b) moment profiles at two distinct load lateral levels – *F* = 90, 175 kN.
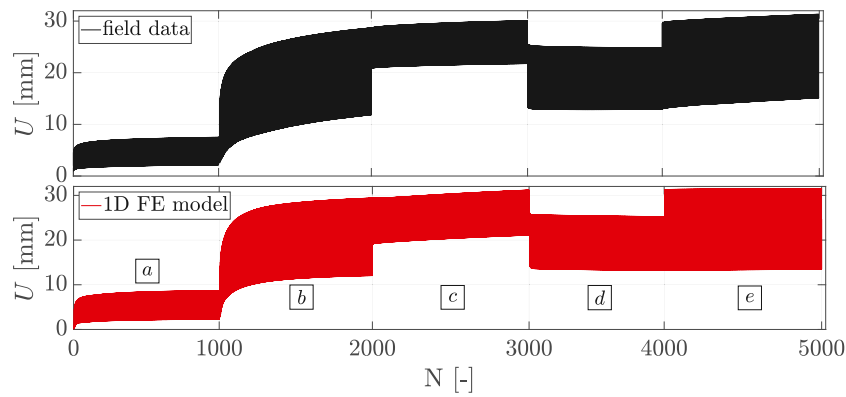

Fig. 16. Measured (top) and calculated (bottom) evolution of the lateral pile displacement at ground level for parcels *a − e*.
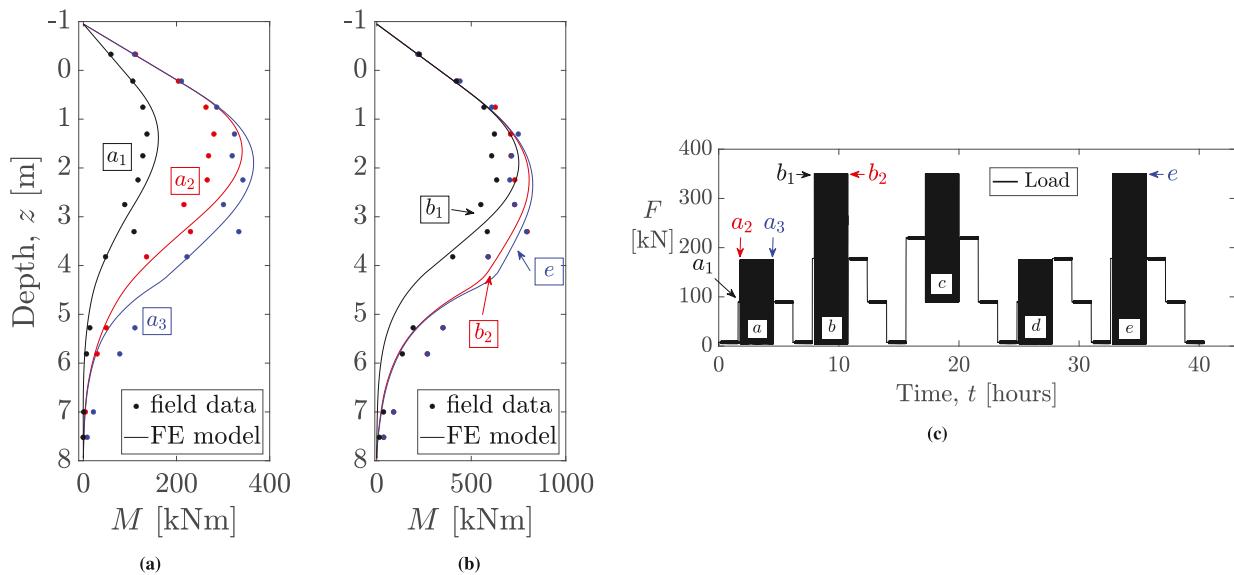

Fig. 17. (a)–(b) Measured (dots) and calculated (solid lines) bending moment profiles; (c) times at which bending moment profiles were measured/calculated along the reference loading programme — each cyclic parcel (*a − e*) features 1000 loading cycles.

The 1D model performance appears to be fully satisfactory also when assessed in terms of displacement accumulation trends (Fig. 16). The evolution per cycle of the pile displacement minima and maxima (and therefore of the associated average cyclic stiffness $K_{cyc}^{av} = (F_{max} - F_{min})/(U_{max} - U_{min})$) are in satisfactory agreement with field measurements. In particular, the peculiar displacement relaxation observed during parcel d is spontaneously simulated by the model, in a fashion similar to the data presented by Kementzetzidis et al. (2022)). Owing to the memory mechanism in the memory elements, the resulting $p - y$ formulation can also reproduce load history effects in the displacement accumulation rate — and particularly its drastic reduction under loading amplitudes that do not exceed the maximum load experienced by the pile in its previous loading history.

As for the simulation of bending moment profiles (Fig. 17), the following conclusions may be drawn:

- the evolution of the moment profiles along the loading history is reasonably well-captured, especially in the upper half of the embedded pile length;
- in agreement with field measurements, the 1D model simulates upon cycling a gradual increase in the maximum bending moment, as well as its slight shift towards deeper pile locations.
- the simulated bending moments along the deepest third of pile tend to be less accurate than in the upper portion of the pile, especially after the earliest a_1 and a_2 isochrones associated with parcel a (Fig. 17(b)).

Better agreement between measurements and simulation results could be obtained by including additional moment fixity at the pile base — this probably played some role also for the reference test pile, which is was relatively stubby though still quite flexible. As previously mentioned, such addition was not pursued to limit the number of free model parameters with only limited independent data available for calibration. Further, a closer observation of the measured bending moments in Fig. 17 suggests a possibly imperfect performance of some strain gauges, which would make the comparison between recorded and calculated moments somewhat less meaningful at those locations.

5. Concluding remarks

The formulation, calibration, and application of a new $p - y$ model for cyclically loaded piles have been presented in this study. Particularly, the proposed model has been built to extend to cyclic loading conditions the previous monotonic, CPT-based $p - y$ formulation by Suryasentana and Lehane (2016), with the inclusion of (i) a ratcheting control mechanism and (ii) additional soil reaction elements for the detailed modelling of pile–soil gapping effects. Owing to such features, the model can realistically simulate the ratcheting behaviour of the pile head under lateral cyclic loading, along with the peculiar variations in lateral stiffness induced by gapping. Importantly, the main component of the model – formulated in the framework of memory-enhanced bounding surface plasticity – can be calibrated against common CPT data, in a fashion inspired by Suryasentana and Lehane's approach.

The performance of the new $p - y$ model has been assessed against field data from a cyclic loading pile test. In order to quantitatively capture the experimental data (both pile head deflection and bending moment profiles), some adjustments to Suryasentana and Lehane's CPT-based calibration procedure have been introduced likely due to a different range of pile deflection and the neglected influence of additional soil resistance mechanisms (e.g., distributed moments, base shear resistance and moment fixity) – the predictive capabilities of the SL model have already been demonstrated in Li et al. (2015), Suryasentana and Lehane (2014a, 2016) and Anusic et al. (2019). Further, gap-related parameters had to be calibrated by trial-and-error, due to the lack of fully reliable information regarding real in-situ soil reactions.

Overall, the model has been shown to possess very promising predictive potential, as well as to enable efficient analyses of cyclically loaded piles. Future work on the subject will be devoted to three important aspects: (i) extension to clayey soils, featuring inherent cohesive behaviour even when fully saturated; (ii) inclusion of additional soil resisting mechanisms for more accurate analysis of stubby monopiles; (iii) development of a more comprehensive CPT-based calibration procedure, based on additional experimental data and detailed 3D FE studies.

CRediT authorship contribution statement

Evangelos Kementzetzidis: Conceptualisation, Methodology, Software, Validation, Formal analysis, Data curation, Writing – original draft. **Federico Pisanò:** Conceptualisation, Methodology, Supervision, Writing – review & editing. **Andrei V. Metrikine:** Funding acquisition, Project administration, Writing – review & editing.

Declaration of competing interest

Acknowledgements

Appendix A. Derivation of evolution laws for memory internal variables

Specific evolution laws for the memory internal variables, p_M and $p_{\alpha,M}$ in Eq. (13), were derived by adapting the same assumptions made by Liu et al. (2019) to the simpler case of a 1D soil reaction model. It is also worth recalling the following important assumption: the evolution laws that are first derived for virgin loading, are then held valid for any loading conditions (i.e., also for $p \neq \tilde{p}_M$).

A.1. Memory locus expansion

In order to enforce assumed constraints on the evolution of the memory locus ($F^M = 0$), the differential of the memory function F^M with respect to its independent variables is first obtained as follows:

$$dF^M = \frac{\partial F^M}{\partial p} dp + \frac{\partial F^M}{\partial p_{\alpha,M}} dp_{\alpha,M} + \frac{\partial F^M}{\partial p_M} dp_M =$$

$$\text{sgn}(p - p_{\alpha,M}) \cdot dp - \text{sgn}(p - p_{\alpha,M}) \cdot dp_{\alpha,M} - dp_M \quad \text{(A.1)}$$

During a virgin loading event (i.e., starting from $p = \tilde{p}_M$), the boundary of the memory locus that coincides with the current stress point (henceforth, point A) is considered to be dragged along the load increment while the opposite boundary (point B) is kept fixed. Analytically, this

assumption translates into requiring $dF^M(B) = 0$ with $dp(B) = 0$, i.e., based on Eq. (A.1):

$$dF^M(B) = 0 =$$

$$- \text{sgn}(p_B - p_{\alpha,M}) \cdot dp_{\alpha,M} - dp_M \tag{A.2}$$

and therefore to the following increment of the memory locus size:

$$dp_M = |dp_{\alpha,M}| \tag{A.3}$$

A.2. Memory locus translation

It has been shown in Section 2.1 how the translation of the vanishing yield locus (i.e., with $dp_\alpha \equiv dp$) takes place along the direction of the plastic displacement increment (with $\text{sgn}(dy_p) \equiv \text{sgn}(dy) \equiv \text{sgn}(dp)$) in proportion to the distance $|\bar{p}_u - p|$ – see Eqs. (6), (8), and (10). Similarly, the memory locus is assumed to translate along the direction of $\text{sgn}(dp_{\alpha,M}) = \text{sgn}(dy)$ with incremental magnitude proportional to $|\bar{p}_u - \tilde{p}_M|$. The expression of the associated 'dummy' hardening modulus $\tilde{H}_M$ in Eq. (16) can be first derived under virgin loading conditions – i.e., when $p \equiv \tilde{p}_M$ – in combination with the condition set by Eq. (A.3):

$$dp = d\tilde{p}_M = dp_{\alpha,M} + dp_M \cdot \text{sgn}(dy) =$$

$$= 2 \, dp_{\alpha,M} \tag{A.4}$$

Using Eq. (A.4) it is possible to relate the two translation rules for the memory locus (Eq. (16)) and the vanishing yield locus (Eqs. (6) and (10)), which in turn leads to the following relationship between the 'dummy' and the 'real' hardening moduli:

$$\tilde{H}_M = \frac{1}{2} H_M \tag{A.5}$$

Eq. (A.5), strictly applicable only to virgin loading, is finally extended to arbitrary loading conditions to enable the determination of $dp_{\alpha,M}$ by combining Eqs. (A.5)–(16):

$$\tilde{H}_M = \frac{1}{2} \cdot \frac{\alpha \cdot m}{D} \cdot |\bar{p}_u - \tilde{p}_M| \cdot \left| \frac{1}{\alpha} \ln \left(\frac{\bar{p}_u - \tilde{p}_M}{\bar{p}_u - p_0} \right) \right|^{\frac{m-1}{m}} \tag{A.6}$$

Appendix B. Calibration of the closure spring parameter α_c in Eq. (19)

The inspection of the field data shown in Section 4 (Figs. 13(a), 14) suggests an increasing displacement relaxation for increasing $|y_{max}|$, i.e., the minimum and the maximum pile head displacements evolve at substantially different rates (the former more slowly than the latter). This feature is incorporated in the model through the formulation of the closure spring, particularly by updating either α_c or m_c (shape parameters) upon each resetting of the gap configuration, i.e., upon unloading from the latest y_{max}. By rewriting Eq. (19) as:

$$Bp_{c,max} = p_{c,max} \exp\{-\alpha_c A^{m_c}\} \tag{B.1}$$

and solving for α_c

$$B = \exp\{-\alpha_c(A)^{m_c}\} \Rightarrow a_c = -\frac{\ln B}{A^{m_c}} \tag{B.2}$$

it is possible to impose for every reconfiguration of the gap (unloading from the latest y_{max}), the deformation of the gap spring ($\Delta y_g = |y_g - y_{g,0}|$) required for the transition $p_{c,max} \rightarrow Bp_{c,max}$ ($0 < B < 1$), or backwards ($Bp_{c,max} \rightarrow p_{c,max}$). Setting $\Delta y_g = A|y_{max}|$ enables the simulation of the observed enhancement in relaxation (decrease of the average stiffness $|p_{c,max} - Bp_{c,max}| / |Ay_{max}|$) with increasing y_{max} ($0 < A < 1$). In essence, the recalibration of α_c based on $|y_{max}|$ essentially tunes the average closure spring stiffness to fit the field data – $B = 0.15$ and $A = 0.55$ have been used throughout this work.

References

Abadie, C.N., 2015. Cyclic lateral loading of monopile foundations in cohesionless soils (DPhil thesis). University of Oxford.

Abadie, C.N., Byrne, B.W., Houlsby, G.T., 2019. Rigid pile response to cyclic lateral loading: Laboratory tests. Géotechnique 69, 863–876.

Achmus, M., Kuo, Y.-S., Abdel-Rahman, K., 2009. Behavior of monopile foundations under cyclic lateral load. Comput. Geotech. 36, 725–735.

Albiker, J., Achmus, M., Frick, D., Flindt, F., 2017. 1g model tests on the displacement accumulation of large-diameter piles under cyclic lateral loading. Geotech. Test. J. 40, 173–184.

Anusic, I., Lehane, B.M., Eiksund, G.R., Liingaard, M.A., 2019. Influence of installation method on static lateral response of displacement piles in sand. Geotech. Lett. 9, 193–197.

API (American Petroleum Institute), 2011. 2GEO (2011). Recommended practice for geotechnical foundation design consideration. API Washington, DC, USA.

Arany, L., Bhattacharya, S., Macdonald, J., Hogan, S.J., 2017. Design of monopiles for offshore wind turbines in 10 steps. Soil Dyn. Earthq. Eng. 92, 126–152.

Bea, R.G., Audibert, J.M.E., Akky, M.R., 1979. Earthquake response of offshore platforms. J. Struct. Div. 105.

Beuckelaers, W., Burd, H., Houlsby, G., McAdam, R., Byrne, B., 2020. A generalised winkler model for the hysteretic and ratcheting behaviour of monopiles in clay and sand. In: Westgate, Z. (Ed.), Frontiers in Offshore Geotechnics IV: Proceedings of the 4th International Symposium on Frontiers in Offshore Geotechnics (ISFOG 2020). pp. 1263–1272, Austin, Texas, USA.

Borja, R.I., Amies, A.P., 1994. Multiaxial cyclic plasticity model for clays. J. Geotech. Eng. 120, 1051–1070.

Boulanger, R.W., Curras, C.J., Kutter, B.L., Wilson, D.W., Abghari, A., 1999. Seismic soil-pile-structure interaction experiments and analyses. J. Geotech. Geoenviron. Eng. 125, 750–759.

Boulanger, R.W., Kutter, B.L., Wilson, D.W., 1998. Pile Foundations in Liquefied and Laterally Spreading Ground During Earthquakes: Centrifuge Experiments & Analyses. Technical Report, University of California, Davis, Center for Geotechnical Modeling, Department of Civil and Environmental Engineering.

Brandenberg, S.J., Zhao, M., Boulanger, R.W., Wilson, D.W., 2013. p-y plasticity model for nonlinear dynamic analysis of piles in liquefiable soil. J. Geotech. Geoenviron. Eng. 139, 1262–1274.

Burd, H.J., Taborda, D.M.G., Zdravković, L., Abadie, C.N., Byrne, B.W., Houlsby, G.T., Gavin, K.G., Igoe, D.J., Jardine, R.J., Martin, C.M., et al., 2020. PISA design model for monopiles for offshore wind turbines: Application to a marine sand. Géotechnique 70, 1048–1066.

Byrne, B.W., Aghakouchak, A., Buckley, R.M., Burd, H.J., Gengenbach, J., Houlsby, G.T., McAdam, R.A., Martin, C.M., Schranz, F., Sheil, B.B., Suryasentana, S.K., 2020a. PICASO: Cyclic lateral loading of offshore wind turbine monopiles. In: Westgate, Z. (Ed.), Frontiers in Offshore Geotechnics IV: Proceedings of the 4th International Symposium on Frontiers in Offshore Geotechnics (ISFOG 2020). pp. 1526–1535, Austin, Texas, USA.

Byrne, B.W., Burd, H.J., Zdravkovic, L., Abadie, C.N., Houlsby, G.T., Jardine, R.J., Martin, C.M., McAdam, R.A., Pacheco Andrade, M., Pedro, A.M., et al., 2019. PISA design methods for offshore wind turbine monopiles. In: Offshore Technology Conference, Houston, Texas, USA.

Byrne, B.W., McAdam, R.A., Beuckelaers, W.J., Burd, H.J., Gavin, K., Houlsby, G.T., Igoe, D.J.P., Jardine, R., Martin, C.M., 2020b. Cyclic laterally loaded medium scale field pile testing for the PISA project. In: Westgate, Z. (Ed.), Frontiers in Offshore Geotechnics IV: Proceedings of the 4th International Symposium on Frontiers in Offshore Geotechnics (ISFOG 2020). pp. 1323–1332, Austin, Texas, USA.

Choi, J.I., Kim, M.M., Brandenberg, S.J., 2015. Cyclic p-y plasticity model applied to pile foundations in sand. J. Geotech. Geoenviron. Eng. 141, 04015013.

Corti, R., Diambra, A., Wood, D.M., Escribano, D.E., Nash, D.F., 2016. Memory surface hardening model for granular soils under repeated loading conditions. J. Eng. Mech. 142, 04016102.

Cuéllar, P., Baeßler, M., Rücker, W., 2009. Ratcheting convective cells of sand grains around offshore piles under cyclic lateral loads. Granul. Matter 11, 379.

Cuéllar, P., Georgi, S., Baeßler, M., Rücker, W., 2012. On the quasi-static granular convective flow and sand densification around pile foundations under cyclic lateral loading. Granul. Matter 14, 11–25.

Dafalias, Y.F., 1986. Bounding surface plasticity. I: Mathematical foundation and hypoplasticity. J. Eng. Mech. 112, 966–987.

Dafalias, Y.F., Popov, E.P., 1977. Cyclic loading for materials with a vanishing elastic region. Nucl. Eng. Des. 41, 293–302.

Dafalias, Y.F., Taiebat, M., 2016. SANISAND-Z: Zero elastic range sand plasticity model. Géotechnique 66, 999–1013.

Davidson, H.L., 1982. Laterally loaded drilled pier research. In: Volume 1: Design Methodology. Final Report [PADLL]. Technical Report, GAI Consultants, Inc., Monroeville, PA (USA).

DNV, 2014. DNV-OS-J101 Offshore Standard: Design of Offshore Wind Turbine Structures. DNV AS, Høvik, Norway.

Dyson, G.J., Randolph, M.F., 2001. Monotonic lateral loading of piles in calcareous sand. J. Geotech. Geoenviron. Eng. 127, 346–352.

Fredlund, D.G., 2006. Unsaturated soil mechanics in engineering practice. J. Geotech. Geoenviron. Eng. 132, 286–321.

Frick, D., Achmus, M., 2019. Model tests on the displacement accumulation of monopiles subjected to general cyclic loading. In: Proceedings of Coastal Structures 2019. Bundesanstalt Für Wasserbau, Karlsruhe.

Gerolymos, N., Gazetas, G., 2005a. Constitutive model for 1-D cyclic soil behaviour applied to seismic analysis of layered deposits. Soils Found. 45, 147–159.

Gerolymos, N., Gazetas, G., 2005b. Phenomenological model applied to inelastic response of soil-pile interaction systems. Soils Found. 45, 119–132.

Gerolymos, N., Gazetas, G., 2006. Development of Winkler model for static and dynamic response of Caisson foundations with soil and interface nonlinearities. Soil Dyn. Earthq. Eng. 26, 363–376.

Hededal, O., Klinkvort, R.T., et al., 2010. A new elasto-plastic spring element for cyclic loading of piles using the py curve concept. In: Benz, T., Nordal, S. (Eds.), Numerical Methods in Geotechnical Engineering. NUMGE 2010, Taylor & Francis, Trondheim, Norway, pp. 883–888.

Heidari, M., El Naggar, H., Jahanandish, M., Ghahramani, A., 2014. Generalized cyclic p–y curve modeling for analysis of laterally loaded piles. Soil Dyn. Earthq. Eng. 63, 138–149.

Hutchinson, J.R., 2001. Shear coefficients for Timoshenko beam theory. J. Appl. Mech. 68, 87–92.

Jamiolkowski, M., Lo Presti, D.C.F., Manassero, M., 2003. Evaluation of relative density and shear strength of sands from CPT and DMT. In: Germaine, J.T., Sheahan, T.C., Whitman, R.V. (Eds.), Symposium on Soil Behavior and Soft Ground Construction Honoring Charles C. "Chuck" Ladd. Boston, Massachusetts, pp. 201–238.

Jostad, H.P., Grimstad, G., Andersen, K.H., Saue, M., Shin, Y., You, D., 2014. A FE procedure for foundation design of offshore structures–applied to study a potential OWT monopile foundation in the Korean Western sea. Geotech. Eng. J. SEAGS AGSSEA 45, 63–72.

Kaynia, A.M., 2021. Analysis of Pile Foundations Subject to Static and Dynamic Loading. CRC Press, Leiden, The Netherlands.

Kementzetzidis, E., Corciulo, S., Versteijlen, W.G., Pisanò, F., 2019. Geotechnical aspects of offshore wind turbine dynamics from 3D non-linear soil-structure simulations. Soil Dyn. Earthq. Eng. 120, 181–199.

Kementzetzidis, E., Metrikine, A., Versteijlen, W., Pisanò, F., 2021. Frequency effects in the dynamic lateral stiffness of monopiles in sand: insight from field tests and 3D FE modelling. Géotechnique 71, 812–825.

Kementzetzidis, E., Pisanò, F., Elkadi, A.S.K., Tsouvalas, A., Metrikine, A.V., 2022. Gentle driving of piles at a sandy site combining axial and torsional vibrations: cyclic/dynamic lateral loading tests. submitted for publication.

Kementzetzidis, E., Versteijlen, W.G., Nernheim, A., Pisanò, F., 2018. 3D FE dynamic modelling of offshore wind turbines in sand: Natural frequency evolution in the pre-to after-storm transition. In: Numerical Methods in Geotechnical Engineering IX, vol. 2, CRC Press, pp. 1477–1484.

Klinkvort, R.T., 2012. Centrifuge Modelling of Drained Lateral Pile-Soil Response (Ph.D. thesis). Technical University of Denmark, DTU Civil Engineering.

Klinkvort, R.T., Leth, C.T., Hededal, O., 2010. Centrifuge modelling of a laterally cyclic loaded pile. In: Springman, S., Laue, J., Seward, L. (Eds.), Proceedings of the 7th International Conference on Physical Modelling in Geotechnics. ICPMG 2010, CRC press, Zurich, Switzerland, pp. 959–964.

Lam, I.P.O., Martin, G.R., 1986. Seismic Design of High-Way Bridge Foundations. Technical Report. Report No. FHWA/RD-86/102, US Department of Transportation.

LeBlanc, C., Houlsby, G.T., Byrne, B.W., 2010. Response of stiff piles in sand to long-term cyclic lateral loading. Géotechnique 60, 79–90.

Li, W., Igoe, D., Gavin, K., 2014. Evaluation of CPT-based p–y models for laterally loaded piles in siliceous sand. Géotechnique Lett. 4, 110–117.

Li, W., Igoe, D., Gavin, K., 2015. Field tests to investigate the cyclic response of monopiles in sand. Proc. Inst. Civ. Eng. Geotech. Eng. 168, 407–421.

Liu, H.Y., Abell, J.A., Diambra, A., Pisanò, F., 2019. Modelling the cyclic ratcheting of sands through memory- enhanced bounding surface plasticity. Géotechnique 69, 783–800.

Liu, H., Diambra, A., Abell, J.A., Pisanò, F., 2020. Memory-enhanced plasticity modeling of sand behavior under undrained cyclic loading. Journal of Geotechnical and Geoenvironmental Engineering 146, 04020122.

Liu, H., Kementzetzidis, E., Abell, J.A., Pisanò, F., 2021. From cyclic sand ratcheting to tilt accumulation of offshore monopiles: 3D FE modelling using SANISAND-MS. Géotechnique.

Liu, H., Pisanò, F., Jostad, H.P., Sivasithamparam, N., 2022. Impact of cyclic strain accumulation on the tilting behaviour of monopiles in sand: An assessment of the Miner's rule based on SANISAND-MS 3D FE modelling. Ocean Eng. 250, 110579.

Matlock, H., 1970. Correlation for design of laterally loaded piles in soft clay. In: Offshore Technology Conference. OnePetro.

Matlock, H., Foo, S.H.C., et al., 1978. Simulation of lateral pile behavior under earthquake motion. In: Earthquake Engineering and Soil Dynamics–Proceedings of the ASCE Geotechnical Engineering Division Specialty Conference, June 19-21, 1978, Pasadena, California. Sponsored By Geotechnical Engineering Division of ASCE in Cooperation with, vol. 1.

McKenna, F., 2011. OpenSees: A framework for earthquake engineering simulation. Comput. Sci. Eng. 13, 58–66.

Metrikine, A., Tsouvalas, A., Segeren, M., Elkadi, A., Tehrani, F., Gómez, S., Atkinson, R., Pisanò, F., Kementzetzidis, E., Tsetas, A., Molenkamp, T., van Beek, K., P, D., 2020. GDP: A new technology for gentle driving of monopiles. In: Westgate, Z. (Ed.), Frontiers in Offshore Geotechnics IV: Proceedings of the 4th International Symposium on Frontiers in Offshore Geotechnics (ISFOG 2020). pp. 736–745, Austin, Texas, USA.

Niemunis, A., Wichtmann, T., Triantafyllidis, T., 2005. A high-cycle accumulation model for sand. Comput. Geotech. 32, 245–263.

Nogami, T., Otani, J., Konagai, K., Chen, H.-L., 1992. Nonlinear soil-pile interaction model for dynamic lateral motion. J. Geotech. Eng. 118, 89–106.

Novello, E.A., 1999. From static to cyclic py data in calcareous sediments. In: Al-Shafei, K.A. (Ed.), Proc. 2nd Int. Conf. on Engineering for Calcareous Sediments. Balkema, Bahrain, pp. 17–27.

Pisanò, F., 2019. Input of advanced geotechnical modelling to the design of offshore wind turbine foundations. In: Sigursteinsson, H., Erlingsson, S., Bessason, B. (Eds.), Proceedings of 17th European Conference on Soil Mechanics and Geotechnical Engineering. ECSMGE2019, International Society of Soil Mechanics and Geotechnical Engineering (ISSMGE), Reykjavík, Iceland, pp. 272–297.

Pisanò, F., Askarinejad, A., Wang, H., Maghsoodi, S., Gavin, K.G., Segeren, M.L.A., Elkadi, A.S.K., de Lange, D., Konstadinou, M., 2022. MIDAS: Monopile improved design through advanced cyclic soil modelling. In: Rahman, M., Jaska, M. (Eds.), Proceedings of 20th International Conference on Soil Mechanics and Geotechnical Engineering (ICSMGE2022). Australian Geomechanics Society, Sydney, Australia, pp. 2677–2682.

Pisanò, F., Jeremić, B., 2014. Simulating stiffness degradation and damping in soils via a simple visco-elastic–plastic model. Soil Dyn. Earthq. Eng. 63, 98–109.

Pyke, R.M., 1979. Nonlinear soil models for irregular cyclic loadings. J. Geotech. Eng. Div. 105, 715–726.

Randolph, M.F., Gourvenec, S., 2011. Offshore Geotechnical Engineering. CRC Press, London.

Richards, I., 2019. Monopile Foundations Under Complex Cyclic Lateral Loadings (DPhil Thesis). University of Oxford.

Richards, I., Bransby, M., Byrne, B., Gaudin, C., Houlsby, G., 2021. Effect of stress level on response of model monopile to cyclic lateral loading in sand. J. Geotech. Geoenviron. Eng. 147, 04021002.

Rudolph, C., Bienen, B., Grabe, J., 2014. Effect of variation of the loading direction on the displacement accumulation of large-diameter piles under cyclic lateral loading in sand. Can. Geotech. J. 51, 1196–1206.

Sloan, S.W., Abbo, A.J., Sheng, D., 2001. Refined explicit integration of elastoplastic models with automatic error control. Eng. Comput. 18, 121–154, No. 1/2.

Staubach, P., Wichtmann, T., 2020. Long-term deformations of monopile foundations for offshore wind turbines studied with a high-cycle accumulation model. Comput. Geotech. 124, 103553.

Suryasentana, S., Lehane, B.M., 2014a. Verification of numerically derived CPT based py curves for piles in sand. In: Ryshkov, I., Isaev, O. (Eds.), Proceedings of 3rd International Symposium on Cone Penetration Testing. Las Vegas, Nevada, USA, pp. 3–29.

Suryasentana, S.K., Lehane, B.M., 2014b. Numerical derivation of CPT-based p–y curves for piles in sand. Géotechnique 64, 186–194.

Suryasentana, S.K., Lehane, B.M., 2016. Updated CPT-based p–y formulation for laterally loaded piles in cohesionless soil under static loading. Géotechnique 66, 445–453.

Suzuki, Y., Nakai, S., 1985. Behavior of a pile under horizontal cyclic loading. In: International Conference on Soil Mechanics and Foundation Engineering, vol. 11, pp. 1413–1416.

Timoshenko, S.P., 1921. LXVI. On the correction for shear of the differential equation for transverse vibrations of prismatic bars. Lond. Edinb. Dublin Philos. Mag. J. Sci. 41, 744–746.

Truong, P., Lehane, B.M., Zania, V., Klinkvort, R.T., 2019. Empirical approach based on centrifuge testing for cyclic deformations of laterally loaded piles in sand. Géotechnique 69, 133–145.

Tsetas, A., Gómez, S., Tsouvalas, A., Kementzetzidis, E., Molenkamp, T., Elkadi, A., Pisanò, F., Metrikine, A., 2022. Gentle driving of piles at a sandy site combining axial and torsional vibrations: Installation tests. submitted for publication.

Wang, L.Z., Wang, H., Zhu, B., Hong, Y., 2018. Comparison of monotonic and cyclic lateral response between monopod and tripod bucket foundations in medium dense sand. Ocean Eng. 155, 88–105.

Wang, H., van Zanten D, V., de Lange, D., Pisanò, F., Gavin, K., Askarinejad, A., 2022. Centrifuge study on the CPT based p-y models for the monopiles. In: The 5th International Symposium on Cone Penetration Testing. CPT'22. Bologna, Italy.

Wichtmann, T., Niemunis, A., Triantafyllidis, T., 2005. Strain accumulation in sand due to cyclic loading: Drained triaxial tests. Soil Dyn. Earthq. Eng. 25, 967–979.

Wichtmann, T., Niemunis, A., Triantafyllidis, T., 2010. Strain accumulation in sand due to drained cyclic loading: On the effect of monotonic and cyclic preloading (Miner's rule). Soil Dyn. Earthq. Eng. 30, 736–745.

Winkler, E., 1867. Die Lehre von der Elasticitaet und Festigkeit: Mit Besonderer Rücksicht auf ihre Anwendung in der Technik, für Polytechnische Schulen, Bauakademien, Ingenieure, Maschinenbauer, Architecten, etc. H. Dominicus.

Zhu, B., Li, T., Xiong, G., Liu, J.C., 2016. Centrifuge model tests on laterally loaded piles in sand. Int. J. Phys. Modell. Geotech. 16, 160–172.